

A 3D model based on elastoplasticity and damage for the modeling of masonry interfaces structures under combined tensile, compressive and shear solicitation

Alexis Blaise TALLA SIMO, Francesco MESSALI & J.G. ROTs

Faculty of Civil Engineering & Geosciences, TU Delft, Delft, The Netherlands

KEY WORDS

Masonry structure

Damage – plastic model

Secant unloading

Interface model

Cyclic loading

FE model

Nonlinear analysis

ABSTRACT

In this paper, we propose a new constitutive model based on elastoplasticity and damage to model the interface of masonry structures under the combined action of tension, compression and shear stresses. To do this, the model is built within the framework of the finite element method for 2D and 3D interfaces. A secant unloading is adapted in tension to limit the plastic deformation and thus be close to the experimental results. To optimize the solution of the nonlinear problem posed and thus limit the convergence problems, we algorithmically decomposed the problem into a damage problem on the one hand and a plasticity problem on the other hand.

For the elasticity criteria, we used 3 threshold surfaces for the three solicitations (cut off in tension, Coulomb for shear and Cap model for compression). We have also introduced two damage variables: one for compression and another for tension/shear coupling.

The model thus constructed was implemented in the commercial finite element software DIANA, and then validated on simple and scaled tests of the structure against experimental results with monotonic and cyclic loadings.

In addition, a particular emphasis was placed on the influence of the different parameters of the model.

1 Introduction:

Masonry, one of the oldest structural materials, is the foundation of both historic monuments around the world and modern residential buildings. These structures are nowadays exposed to natural hazards such as ageing, dynamic impacts and earthquakes. Nonlinear analyses are crucial to study their structural response to such hazard, and accurate constitutive models are therefore key to investigate their resilience and extend their sustainability, preserving our heritage for future generations [1], [2], [3].

However, masonry mechanics has not been completely explored yet, often based on models developed for concrete [4], [5] adapted to reflect the heterogeneous, discontinuous and orthotropic behavior of masonry. With the advancement of research, masonry-specific models, based on the principles of plasticity, damage and thermodynamics, are increasingly being developed.

Thanks to research conducted in the past three decades masonry offers a variety of modeling strategies that fit into both the finite element method (FEA) [6], [7], [8] and discrete element method (DEM) [9], [10], [11]. These modeling strategies can be classified into block-based modeling, continuum homogeneous models, geometry-based models, and equivalent frame models [6], [12]. These modeling strategies can be linked by homogenization [6], [13], [14] or localization techniques established in the context of plasticity, local or non-local damage mechanics, or the coupling of the two.

Block-based models account for the actual masonry texture, as they model explicitly both the units and the mortar joints. The geometry of the latter can be simplified into a line (for 2D models) or a plane (for 3D models), to reduce the computational burden. The experimental results carried out on masonry have shown that the phenomena of masonry fracture occur first at the interface between mortar joints and units [1], [3]. As a

result, block-based models typically lump all the non-linearity at the interface level while the units are modelled as linear elastic elements. The interface nonlinear behavior is modelled either in a plastic framework [6], [7], [15], [16], [17], [18], or damaged [14], [19], [20] or in a combination of the two [21], [22], [23], [24]. A well-known limitation of plasticity-based models relies on the lack of stiffness degradation in case of unloading, which is especially relevant in the cases of cyclic loading. On the opposite, damage-based models often underestimate the cyclic energy dissipation. In this context, the constitutive model introduced in this article is inspired by the well-known model proposed by Lourenço [6], but it is derived in an damaged plasticity framework. This choice allowed to define secant unloading in the case of tensile deformations to properly represent the low residual plastic deformations obtained for tensile loading during experimental tests. The model was initially developed in a two-dimensional framework and then extended in a three-dimensional framework. Note that this model is developed in an isotropic framework, but there are also models in the literature based in the orthotropic framework that are more realistic in terms of the behavior of masonry in different directions [25], [26], [27]

The model adopts three failure surfaces, representing the cut-off, coulomb failure and cap model, for the tensile, shear, and compressive failure, respectively. To minimize the well-known numerical convergence problems caused by the multiplicity of the failure threshold surfaces in the elastoplastic framework, an adaptive sub-step algorithm is implemented into the solving algorithm.

The evolution of the damage variables is expressed in terms of equivalent plastic deformation. The damage and plasticity are assessed and implemented in two separate blocks, which contributes improving the robustness of the model and reduces convergence problems.

The proposed algorithm is implemented in a commercial finite element software (DIANA FEA) via a user define subroutine. The paper introduces the proposed model formulations in Section 2, and its implementation in a finite element software in Section 3. The validation of the model against experimental results at both material and structural level is provided in Section 4, while the concluding remarks are reported in Section 5.

2 Formulation of the interface model with elastoplastic with damage:

2.1 Interface Damage:

The progression of cracks in masonry structures can be characterized by the stress-displacement response at

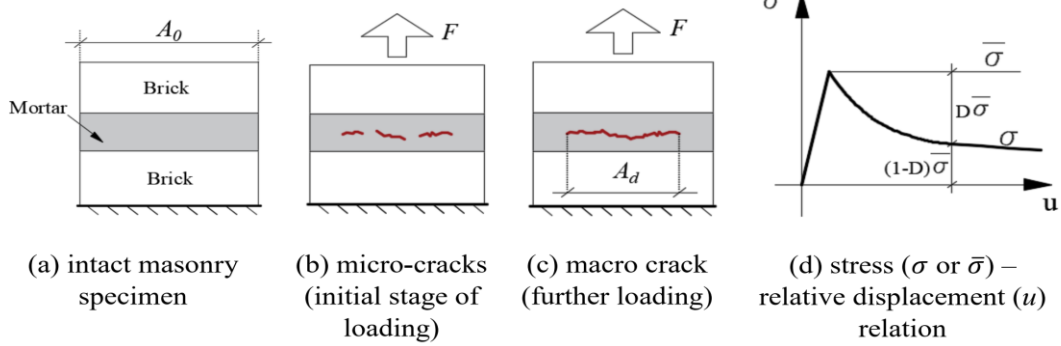


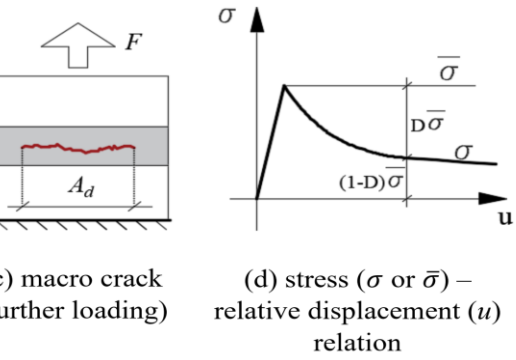
Figure 1 Characterization of Masonry Joint Failure with Nominal and Effective Stresses [22]

The appearance of microcracks hinders the material's additional ability to resist under additional loads, thus manifesting a *hardening phenomenon* in the deformation phase, which is particularly observable under compressive stresses (Figure 1-c). The emergence of macroscopic cracks induces a reduction in the resistance capacity of the

material or mortar, characterized by a *softening behavior* due to deformation (Figure 1-b, c). In the context of tensile and shear loads, the time interval between the onset of microscopic and macroscopic cracks is minimal, leading to an almost insignificant deformation reinforcement zone. In contrast to the nominal stress, which evolves according to the pattern of variation of the force F , the effective stress remains unchanged, undergoing no decrease after the peak load.

the interface. During the initial loading phase after the yield strength, some micro-cracks formed in the mortar matrix and at the interface between the mortar and the bricks. As the load gradually increases, these microcracks increase and join to form macro-cracks (Figure 1-a). The degree of failure in the structure can thus be determined by using a variable called damage, D which represents the ratio of the damaged area or volume to the undamaged surface or volume. For a damaged interface, the effective and nominal stresses are expressed by the following relationships, respectively:

$$\bar{\sigma} = \frac{F}{A_0 - A_d} \quad \sigma = \frac{F}{A_0} = (1 - D)\bar{\sigma}$$



➤ **The 2D interface behavior model results in the following equations:**

$$\begin{Bmatrix} \sigma_n \\ \sigma_s \end{Bmatrix} = \begin{bmatrix} 1 - D_n & 0 \\ 0 & 1 - D_s \end{bmatrix} \begin{Bmatrix} \bar{\sigma}_n \\ \bar{\sigma}_s \end{Bmatrix} \Rightarrow \{\sigma\} = ([\mathbb{I}] - [D])\{\bar{\sigma}\}$$

Similarly, in the elastic domain, the effective stresses are given by the relation:

$$\begin{Bmatrix} \bar{\sigma}_n \\ \bar{\sigma}_s \end{Bmatrix} = \begin{bmatrix} K_n^0 & 0 \\ 0 & K_s^0 \end{bmatrix} \begin{Bmatrix} u_n \\ u_s \end{Bmatrix} \Rightarrow \{\bar{\sigma}\} = [K]\{u\}$$

• **The 3D interface behavior model results in the following equations:**

$$\begin{Bmatrix} \sigma_n \\ \sigma_s \\ \sigma_t \end{Bmatrix} = \begin{bmatrix} 1 - D_n & 0 & 0 \\ 0 & 1 - D_s & 0 \\ 0 & 0 & 1 - D_s \end{bmatrix} \begin{Bmatrix} \bar{\sigma}_n \\ \bar{\sigma}_s \\ \bar{\sigma}_t \end{Bmatrix} \Rightarrow \{\sigma\} = ([\mathbb{I}] - [D])\{\bar{\sigma}\}$$

With σ_n Normal stresses; σ_s and σ_t shear stresses in both directions.

Similarly, in the elastic domain, the effective stresses are given by the relation:

$$\begin{pmatrix} \bar{\sigma}_n \\ \bar{\sigma}_s \\ \bar{\sigma}_t \end{pmatrix} = \begin{bmatrix} K_n^0 & 0 & 0 \\ 0 & K_s^0 & 0 \\ 0 & 0 & K_t^0 \end{bmatrix} \begin{pmatrix} u_n \\ u_s \\ u_t \end{pmatrix} \Rightarrow \{\bar{\sigma}\} = [K]\{u\}$$

2.2 Formulation of the plastic behavior of the interface:

2.2.1 Multi-plastic threshold surface:

To solve the plasticity problem, the failure surfaces corresponding to the considered failure modes must be defined. The following criteria are defined:

- A tension cut-off for tension failure:

$$F_T = \sigma_n - \bar{f}_t(\kappa_1)$$

- An elliptical cap for compression failure:

$$F_C = C_{nn}\sigma_n^2 + C_{ss}\tau + C_n\sigma_n - (\bar{f}_c(\kappa_3))^2$$

- A Coulomb-based criterion for shear failure:

$$F_S = |\tau| + \sigma_n \tan \phi - \bar{f}_s(\kappa_2)$$

Where $\bar{f}_t(\kappa_3)$, $\bar{f}_c(\kappa_3)$ and $\bar{f}_s(\kappa_2)$ are respectively the strength in tension, compression and shear; C_{nn} and C_n the parameters with control the center of the cap and

his intersection with the tensile part of the normal stress axis whereas C_{ss} control the contribution of the shear stress to failure. In this study we will take $C_{nn} = 1$, $C_n = 0$. C_{ss} a constant value often equal to 9 or 3 depending on the properties of the material.

In a 3D framework the shear stress is composed of two components that can be combined into one single component by means of the following relationship:

$$\tau = \sqrt{\sigma_s^2 + \sigma_t^2}$$

A graphical representation of the defined criteria is provided in Figure 2.

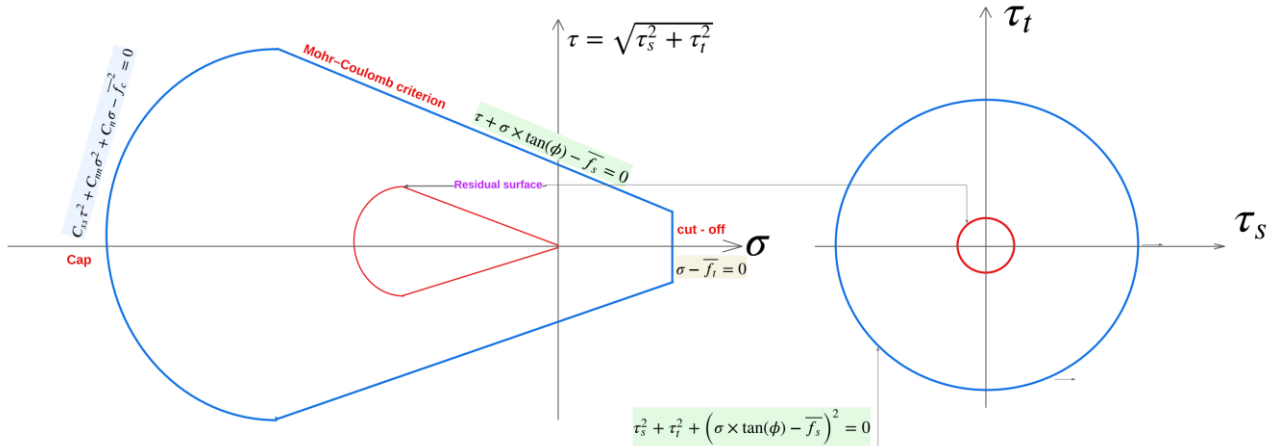
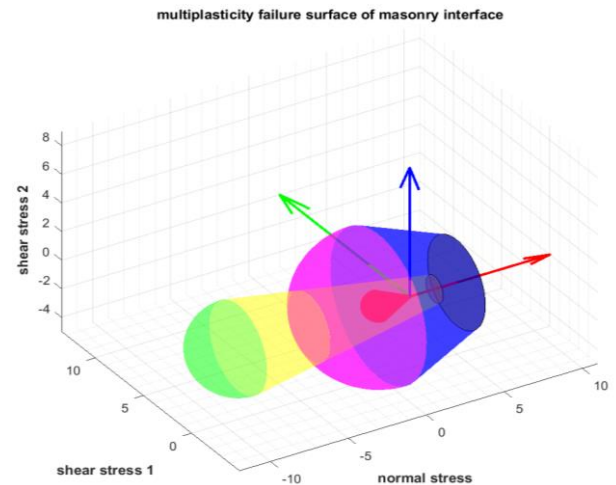


Figure 2 Elastic surface in stress space (a) Three-dimensional surface reduced to the two-dimensional plane (b)

2.2.2 Tensile and shear cyclic behavior:

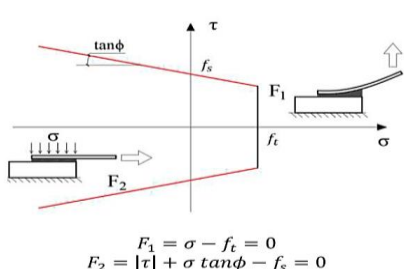


Figure 3 coulomb friction with tension cut-off model

To appropriately consider the normal/tangential behavior of the interface model, not only the uniaxial constitutive response for each of the two regimes needs to be defined in the context of damage plasticity, but also the reciprocal influence must be identified. To

this scope, a Coulomb friction with tension cut-off model is adopted **Figure 3**

The uniaxial tensile (\bar{f}_t) and shear (\bar{f}_s) strength of the interface are defined based on the following formulations:

$$\bar{f}_t = f_t \exp\left(-\frac{f_t}{G_f^I} \kappa_1\right)$$

$$\bar{f}_s = c \exp\left(-\frac{c}{G_f^{II}} \kappa_2\right)$$

Where f_t initial tensile strength, c The cohesion of the interface, G_f^I and G_f^{II} the fracture energy in mode I and II respectively, $\tan \psi$ is the dilatancy. [K] The elastic rigidity matrix of the interface as expressed in equation :

$$[K] = \begin{bmatrix} E & 0 \\ 0 & G \end{bmatrix}_{2D} = \begin{bmatrix} E & 0 & 0 \\ 0 & G & 0 \\ 0 & 0 & G \end{bmatrix}_{3D}$$

While $\tan \phi$ is the coefficient of friction given by:

$$\tan \phi = \tan \phi_0 + (\tan \phi_r - \tan \phi_0) \frac{c - \bar{f}_s}{c}$$

Where $\tan \phi_r$ and $\tan \phi_0$ are residual and initial coefficient of friction respectively.

Variables κ_1 and κ_2 are the internal variables that govern the evolution of damage, whose formulation is based on the equivalent plastic deformation, as expressed by the following relations:

$$\dot{\kappa}_1 = \sqrt{(\dot{\varepsilon}_p)^T \dot{\varepsilon}_p} = \sqrt{\left(\dot{\lambda}_1 \frac{\partial Q_T}{\partial \{\sigma\}}\right)^T \left(\dot{\lambda}_1 \frac{\partial Q_T}{\partial \{\sigma\}}\right)} = \dot{\lambda}_1$$

$$\dot{\kappa}_2 = \sqrt{\left(\dot{\lambda}_2 \frac{\partial Q_S}{\partial \{\sigma\}}\right)^T \left(\dot{\lambda}_2 \frac{\partial Q_S}{\partial \{\sigma\}}\right)} = \dot{\lambda}_2 \sqrt{1 + \tan \psi}$$

Where $\dot{\lambda}_1$ and $\dot{\lambda}_2$ are the plastic multiplier in tension and shear, respectively. It is also considered that the softening behavior is only controlled by the plastic displacement in the shear direction:

$$\dot{\kappa}_2^{n+1} = |\Delta u_s^p| = \dot{\lambda}_2$$

The uniaxial behavior in tension and shear is represented in **Figure 4** and **Figure 5**, respectively.

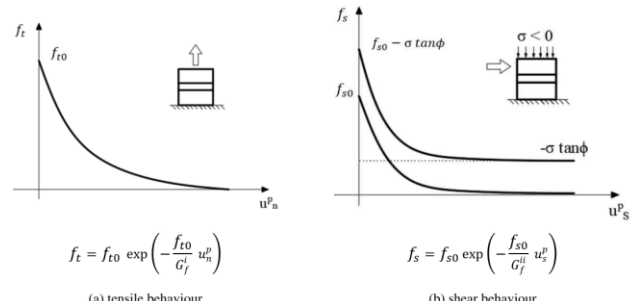


Figure 4 Tensile and shear behavior for exponential softening.

As introduced in Section 1, a tensile secant unloading/reloading path (**Figure 5**) is assumed to align with the experimental outcomes that show the almost complete lack of permanent deformations for uniaxial tensile loading, while keeping a simple formulation.

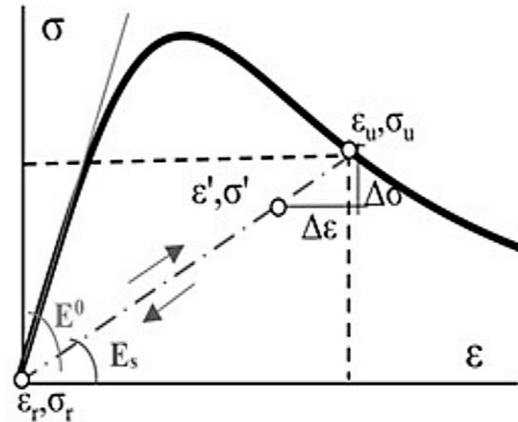


Figure 5 secant unloading/reloading

The secant modulus E_s is given by the stress-strain law by the following equation:

$$E_s = \sigma(\epsilon_u)/\epsilon_u$$

where the unloading strain (ϵ_u) is the maximum strain, the material has ever experienced. It should be noted that despite the simplicity, the secant strategy loses representativity when many cycles are applied during the loading history since the permanent strain are not considered, and consequently any plastic strain cumulation is overlooked.

2.2.3 Coupling between tensile and shear:

To constitute the interface model resulting from the coupling between the shear, we put ourselves within the framework of the linear elasticity developed for the cohesive elements.

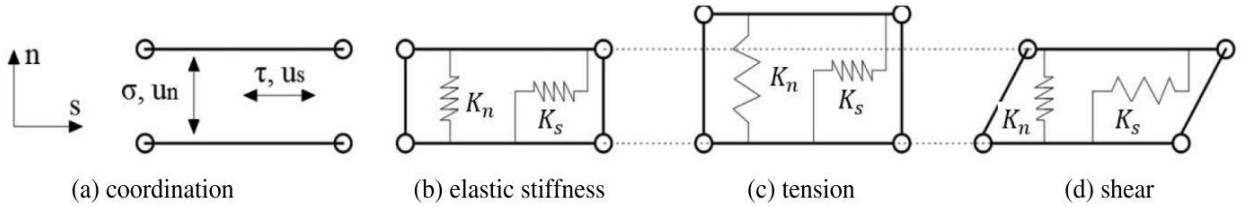


Figure 6 Simplified Diagram of Normal and Tangential Stress

$$\{\sigma\} = [K^0]\{u\} \Rightarrow \begin{pmatrix} \sigma_n \\ \sigma_s \end{pmatrix} = \begin{bmatrix} K_n^0 & 0 \\ 0 & K_s^0 \end{bmatrix} \begin{pmatrix} u_n^{tension} \\ u_s \end{pmatrix}$$

The functions that characterize the threshold surface here will be that of the tension cut-off and the Coulomb criterion. $F_T = \sigma - \bar{f}_t$ $F_S = |\tau| + \sigma \tan \phi - f_s$

When we expanded the previous uncoupled uniaxial expressions, the increments of plastic displacement (shear and tensile) were equal to the related plastic multipliers, respectively.

$$du_n^p = d\kappa_1 = d\lambda_1 \quad du_s^p = d\kappa_2 = d\lambda_2$$

In the case of a linkage, we will use the version proposed by [6] the following relationships:

$$du_n^p = d\kappa_1 = \sqrt{\dot{\lambda}_1^2 + \frac{G_f^{I^2} c^2}{G_f^{II^2} ft^2} \dot{\lambda}_2^2}$$

$$du_s^p = d\kappa_2 = \sqrt{\dot{\lambda}_2^2 + \frac{G_f^{II^2} ft^2}{G_f^{I^2} c^2} \dot{\lambda}_1^2}$$

Both relationships are used when the elastic prediction is in the area at the intersection of the two surfaces (coin). In the case where this prediction is on the side of one or another surface, the uncoupled relationships are automatically reused.

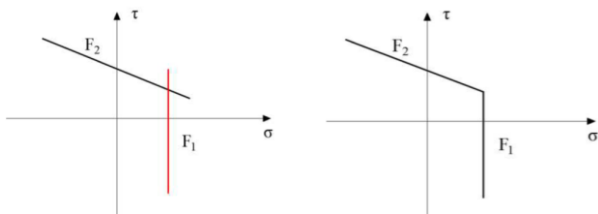


Figure 7 Uncoupled and coupled tension/shear composite surface

2.2.4 Determination of Damage:

Experimentally, we have a coupling between tensile and shear, so we will use the same damage variable for both stresses. We will therefore use a coupling between tensile and shear damage.

- ✓ The tensile damage is given by:

$$\frac{\bar{f}_t}{f_t} = \exp\left(-\frac{f_t}{G_f^I} \kappa_1\right) = 1 - w_t \Rightarrow$$

$$w_t = 1 - \exp\left(-\frac{f_t}{G_f^I} \kappa_1\right)$$

- ✓ The shear damage is given by:

$$\frac{\bar{f}_s}{c} = \exp\left(-\frac{c}{G_f^{II}} \kappa_2\right) = 1 - w_s \Rightarrow$$

$$w_s = 1 - \exp\left(-\frac{f_s}{G_f^{II}} \kappa_2\right)$$

As a result, we propose in this work a coupling between tensile and shear damage at each stage of loading the structure. This coupling results in the following relationship:

$$w(w_s, w_t) = w_t(\kappa_1) + w_s(\kappa_2) - w_t(\kappa_1)w_s(\kappa_2)$$

This relationship guarantees us a limit of the damage between $0 \leq w(w_s, w_t) \leq 1$

w_s And w_t are the shear and tensile damages defined above in uniaxial cases.

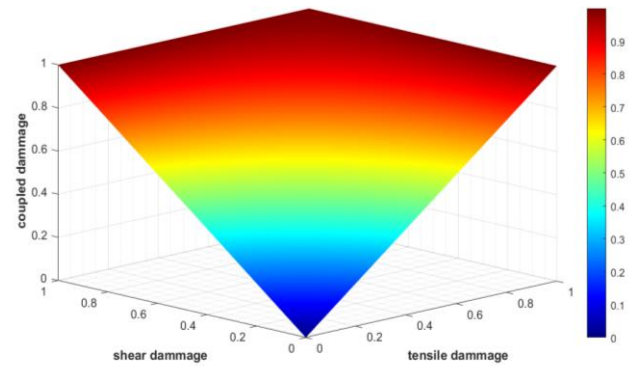


Figure 8 Evolution of three-dimensional damage

2.2.5 Cyclic compression behavior:

- a) Elastic phase: The elastic behavior of the interface in 2D following equation:

$$\{\sigma\} = [K^0]\{u\} \begin{bmatrix} K_n^0 & 0 \\ 0 & K_s^0 \end{bmatrix} \begin{pmatrix} u_n^{compression} \\ u_s \end{pmatrix}$$

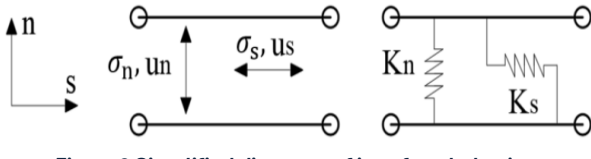


Figure 9 Simplified diagrams of interface behavior

The elliptical elastic surface proposed by [6] which is written:

$$F_C = C_{nn}\sigma_n^2 + C_{ss}\tau^2 + C_n\sigma_n - (\bar{\sigma}(\kappa_3))^2$$

b) Evolution of hardening and softening behavior:

We also adopt the hardening and softening behavior proposed in the figure below. This behavior curve is shown below from the experimental data. Clues i, m, p et r are associated with the initial, average, critical, and residual stresses, respectively.

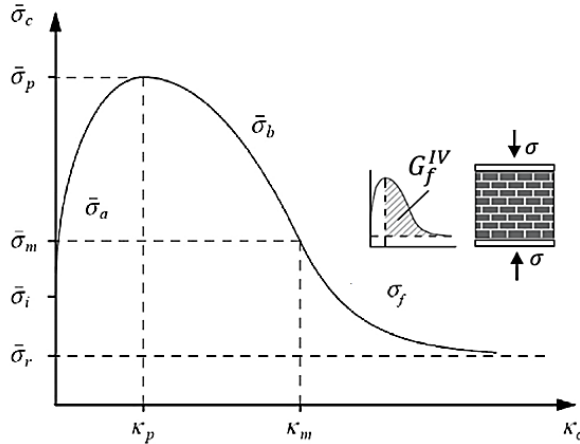


Figure 10 Evolution of compressive strength

$$\left\{ \begin{array}{l} \bar{\sigma}_a(\kappa_3) = \bar{\sigma}_i + (\bar{\sigma}_p - \bar{\sigma}_i) \left[\frac{2\kappa_3}{\kappa_p} - \left(\frac{\kappa_3}{\kappa_p} \right)^2 \right]^\beta \\ \bar{\sigma}_b(\kappa_3) = \bar{\sigma}_p + (\bar{\sigma}_m - \bar{\sigma}_p) \left(\frac{\kappa_3 - \kappa_p}{\kappa_m - \kappa_p} \right)^\alpha \\ \bar{\sigma}_c(\kappa_3) = \bar{\sigma}_r + (\bar{\sigma}_m - \bar{\sigma}_r) \exp \left(m \frac{\kappa_3 - \kappa_m}{\bar{\sigma}_m - \bar{\sigma}_r} \right) \end{array} \right.$$

$$\text{With: } m = 2 \frac{\bar{\sigma}_m - \bar{\sigma}_p}{\kappa_m - \kappa_p} \quad \beta \geq \frac{1}{2} \quad \alpha \geq 2$$

c) Determination of Damage: The amount of damage is derived from the behavior relationship of the evolution of the softening and hardening behavior. We will therefore have two phases of damage, the one during work hardening which is less than 0 and the one during softening which is greater than 0 and which will represent the actual damage in compression.

The ratios of the equivalent plastic deformations are denoted by the following relations:

$$r_{ch} = \frac{\kappa_3}{\kappa_p} \quad r_{cs} = \frac{\kappa_3 - \kappa_p}{\kappa_m - \kappa_p} \quad \text{and} \quad r_{cm} = \frac{\kappa_3 - \kappa_m}{\kappa_m - \kappa_p}$$

We also define the ratio of the stresses to their maximum values. During the first phase (work hardening), the maximum stress value is $\bar{\sigma}_i$. In this case, the damage is deduced D_{ch} :

$$\frac{\bar{\sigma}_a}{\bar{\sigma}_i} = 1 + \left(\frac{\bar{\sigma}_p}{\bar{\sigma}_i} - 1 \right) [2r_{ch} - r_{ch}^2]^\beta = 1 - D_{ch}$$

$$D_{ch} = (1 - \beta_i)[2r_{ch} - r_{ch}^2]^\beta$$

In the second phase, the maximum value of the stress is: $\bar{\sigma}_p$, In this case, the damage is deduced D_{cs} :

$$\frac{\bar{\sigma}_b}{\bar{\sigma}_p} = 1 + \left(\frac{\bar{\sigma}_m}{\bar{\sigma}_p} - 1 \right) r_{cs}^\alpha = 1 - D_{cs} \Rightarrow$$

$$D_{cs} = (1 - \beta_p)r_{cs}^\alpha$$

We assume: $\frac{\bar{\sigma}_m}{\bar{\sigma}_p} = \beta_{mp}$ $\frac{\bar{\sigma}_r}{\bar{\sigma}_p} = \beta_{rp}$ The result is:

$$\frac{\bar{\sigma}_c}{\bar{\sigma}_p} = \frac{\bar{\sigma}_r}{\bar{\sigma}_p} + \left(\frac{\bar{\sigma}_m}{\bar{\sigma}_p} - \frac{\bar{\sigma}_r}{\bar{\sigma}_p} \right) \exp \left(2 \frac{\frac{\bar{\sigma}_m}{\bar{\sigma}_p} - 1}{\frac{\bar{\sigma}_m}{\bar{\sigma}_p} - \frac{\bar{\sigma}_r}{\bar{\sigma}_p}} \frac{\kappa_3 - \kappa_m}{\kappa_m - \kappa_p} \right) =$$

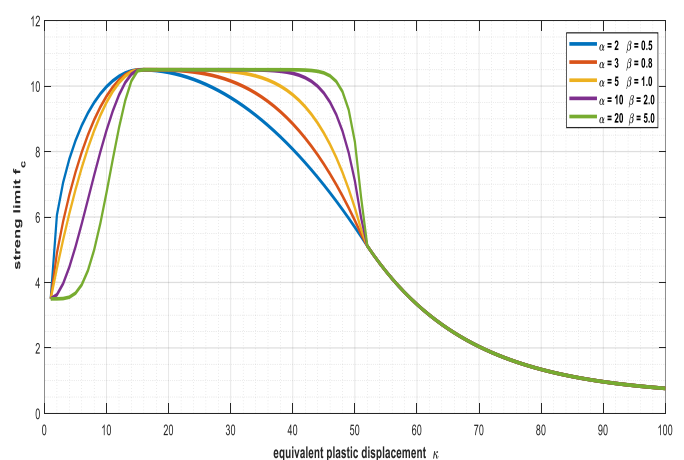
$$\beta_{rp} + (\beta_{mp} - \beta_{rp}) \exp \left(2r_{cm} \frac{\beta_{mp} - 1}{\beta_{mp} - \beta_{rp}} \right) =$$

$$1 - D_{cs} \Rightarrow$$

$$D_{cs} = 1 - \beta_{rp} - (\beta_{mp} - \beta_{rp}) e^{2r_{cm} \frac{\beta_{mp} - 1}{\beta_{mp} - \beta_{rp}}}$$

d) Influence of Elliptical Surface Parameters:

Below, we present the variation of the behavior curve as a function of its parameters β and for the following values α : $\bar{\sigma}_p = f_c = 10,5$; $\bar{\sigma}_i = \frac{f_c}{3} = 3,5$; $\bar{\sigma}_m = \frac{f_c}{2} = 5,25$ and $\bar{\sigma}_r = \frac{f_c}{20} = 0,525$



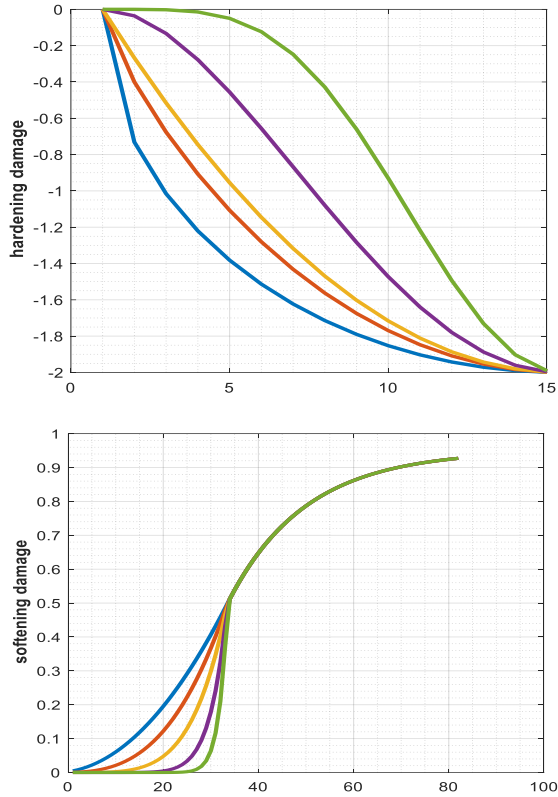


Figure 11 Influence of Compression Parameters on Strength and Damage

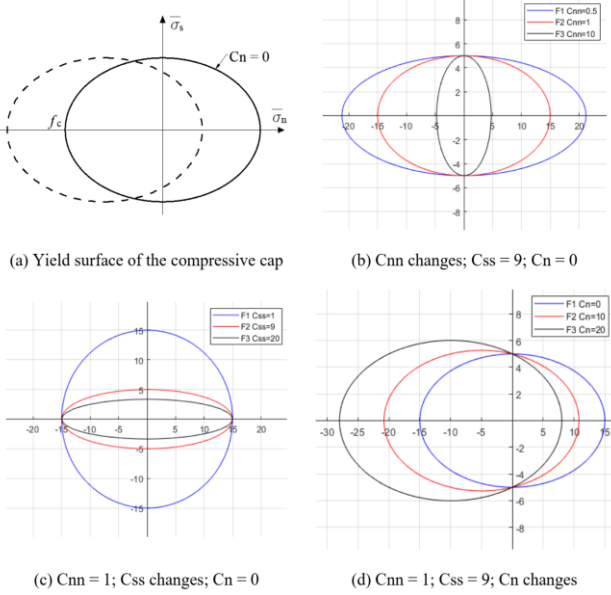


Figure 12 Influence of Cap Model parameters

- e) **Determination of the change variable κ_3** : For the variable κ_3 We have the choice between two solutions: the use of plastic work or equivalent plastic deformation. We will use this second approach:

$$\dot{\kappa}_3 = \sqrt{(\dot{\varepsilon}_p)^T \dot{\varepsilon}_p} = \sqrt{\left(\dot{\lambda}_3 \frac{\partial F_C}{\partial \{\sigma\}} \right)^T \left(\dot{\lambda}_3 \frac{\partial F_C}{\partial \{\sigma\}} \right)}$$

$$\frac{\partial F_C}{\partial \{\sigma\}} = \begin{pmatrix} 2\sigma_n \\ 2C_{ss}\sigma_s \end{pmatrix} \Rightarrow$$

$$\dot{\kappa}_3 = 2\dot{\lambda}_3 \sqrt{(\sigma_n)^2 + (C_{ss}\sigma_s)^2}$$

2.2.6 Coupling between shear and compression:

We assume that there is no physical coupling between compression and shear. This implies that the variable that controls the amount of work hardening, and compression softening remains the same as seen in the uncoupled case. This statement is physically realistic because the shear mode occurs at the joints of the masonry, while the compression mode represents the crushing of the entire masonry. The behavioral equations in this part will then be a coupling of the equations of the simple cases studied previously.

2.3 Numerical implementation:

The retrograde explicit Euler method will be used to determine the set of unknowns of the different problems induced by the previous formulations [28].

In the Framework of this numerical implementation, we note $(*)^n$ and $(*)^{n+1}$ variables in the current step and those updated in the next step respectively. Note also that the constraints used in this part are effective constraints.

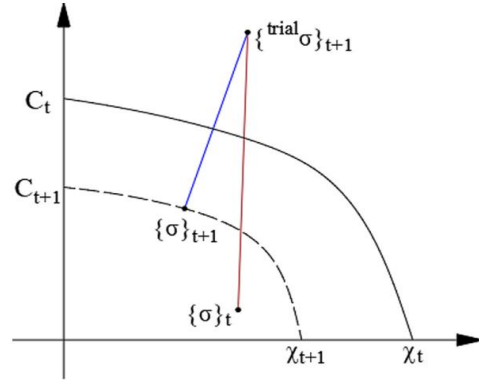


Figure 13 Stress return mapping for backward Euler integration process.

- a) **Elastic Prediction**: In the plane of stresses (normal and tangential), the relationship between the stresses at the preceding and next time is expressed by:

$$\{\sigma\}^{n+1} = \{\sigma\}^n + \{d\sigma\}^{n+1}$$

$$= \{\sigma\}^n + \overbrace{([\mathbb{I} - [D][K]]\{du_e\})}^{[K_1]}$$

$$= \{\sigma\}^n + [K_1]\{du - du_p\}$$

$$\{\sigma\}^{n+1} = \{\sigma^{trial}\}^{n+1} - [K_1]\{du_p\}$$

Where $\{\sigma^{trial}\}^{n+1} = \{\sigma\}^n + [K_1]\{du\}$ is the predicted stress and $[K_1]\{du_p\}$ is the plastic correction.

Considering an unassociated potential, we will have the increment of plastic displacement that will be given by the expression:

$$\{du_p\} = \sum_{i \in \{j_{act}\}} \dot{\lambda}_i \frac{\partial Q_i}{\partial \{\sigma\}}$$

The Index i is relative to the set of surfaces that will be active during the loading of the structure. We will see later how to determine these active surfaces. The elastic prediction will then be:

$$\{\sigma\}^{n+1} = \{\sigma^{trial}\}^{n+1} - [K_1] \sum_{i \in \{j_{act}\}} \dot{\lambda}_i^{n+1} \left(\frac{\partial Q_i}{\partial \{\sigma\}} \right)^{n+1}$$

We postulate an elastic potential of the same shape as the threshold surface in tension, shear and compression:

- ✓ $Q_T = F_T = \sigma_n - f_t$
- ✓ $Q_S = |\tau| + \sigma_n \tan \psi - c$
- ✓ $Q_C = C_{nn} \sigma_n^2 + C_{ss} \tau^2 + C_n \sigma_n - (\bar{\sigma}(\kappa_3))^2$

b) Evolution law: From the potential defined above, the evolution laws are expressed by the following relations to define the plastic deformations in shear, tension and compression:

$$\begin{aligned} du_p^t &= \dot{\lambda}_1 \frac{\partial Q_T}{\partial \sigma_n} = \dot{\lambda}_1 \\ du_p^s &= \dot{\lambda}_2 \frac{\partial Q_S}{\partial \{\sigma\}} = \begin{cases} \dot{\lambda}_2 \frac{\partial Q_S}{\partial \sigma_n} = \dot{\lambda}_2 \tan \psi \\ \dot{\lambda}_2 \frac{\partial Q_S}{\partial \tau} = \dot{\lambda}_2 \frac{\tau^{trial}}{|\tau^{trial}|} \end{cases} \\ du_p^c &= \dot{\lambda}_3 \frac{\partial Q_C}{\partial \{\sigma\}} = \begin{cases} \dot{\lambda}_3 \frac{\partial Q_C}{\partial \sigma_n} = 2\dot{\lambda}_3 \sigma_n \\ \dot{\lambda}_3 \frac{\partial Q_C}{\partial \tau} = 2\dot{\lambda}_3 C_{ss} \tau \end{cases} \end{aligned}$$

By injecting this last equation into the stress expression, we will obtain the updated stress expression. We will thus obtain a set of 5 problems $\varphi_1, \varphi_2, \varphi_3, \varphi_4$ and φ_5 whose number of unknowns will depend on the

loading configuration in which we are located. That problems are define in terms of residues in 7.1.

c) Local iteration strategy: To solve the system of nonlinear equations posed earlier, we need to combine one or two other equations with it so that we can completely determine the unknowns of the problem. For the implementation of the iterative technique, the full consistency condition for the yield functions is used and it is expressed as:

$$F_i = 0 \quad i \in \{j_{act}\}$$

The general form of the set of 5 problems is thus expressed as:

$$\begin{aligned} \{R^j\} &= \begin{pmatrix} R_\sigma^j \\ R_F^j \end{pmatrix} = \\ &\left\{ \begin{array}{l} \{\sigma\}^{n+1} - \{\sigma^{trial}\}^{n+1} + [K_1] \sum_{i \in \{j_{act}\}} \dot{\lambda}_i^{n+1} \left(\frac{\partial Q_i}{\partial \{\sigma\}} \right)^{n+1} \\ F_i^j \end{array} \right\} \end{aligned}$$

d) Resolution of the problem: These problems are implicit in terms of σ_n^{n+1} and τ^{n+1} and $\dot{\lambda}_i$, it will therefore be solved by the Newton–Raphson (NR) iterative method. To simplify the scoring, we note $\{\psi\} = [\sigma_n^{n+1} \quad \tau^{n+1} \quad \dot{\lambda}_i]^T$ the vector bringing together all the unknowns. Linearizing the expression for to order 1, we get:

$$R(\psi^{j+1}) = R(\psi^j + d\psi^{j+1}) \Rightarrow$$

$$R(\psi^{j+1}) = R(\psi^j) + \frac{\partial R(\psi^j)}{\partial \psi^j} d\psi^{j+1} + O[\delta^2]$$

j Is the number of the iteration and the expression $\frac{\partial R(\psi^j)}{\partial \psi^j} = [J]$ is the Jacobian matrix.

Iterative solving of the previous problem involves the exact determination of the Jacobian matrix that will be updated with each iteration. The general form of this Jacobian is given by:

$$[J] = \frac{\partial R(\psi^j)}{\partial \psi^j} = \begin{bmatrix} [I] + \sum_{i \in \{j_{act}\}} \dot{\lambda}_i^{n+1} [K_1] \frac{\partial^2 Q_i}{\partial \{\sigma\}^2} & [K_1] \frac{\partial Q_i}{\partial \{\sigma\}} \\ \left(\frac{\partial F_i}{\partial \{\sigma\}} \right)^T & \left(\frac{\partial F_i}{\partial \dot{\lambda}_i} \right)^T \end{bmatrix}$$

Each Jacobian matrix for the different problem is given in 7.2. Once the plastic multiplier is determined, the internal variables κ_i can be updated by the relationship: $\kappa_i^{n+1} = \kappa_i^n + d\kappa_i^{n+1}$. Subsequently, the damage will also be updated as well as the constraints.

2.4 Searching for Active Surfaces:

As we have seen in the numerical implementation of the couplings above, the difficulty that exists to completely solve the problem is to know which surface(s) will be active at each stage of the loading. In the literature, there are several solutions to overcome this problem. In particular, we will use the approach proposed by [8]. We note $j_{act} = \{i \in \{(1), (2), (3), (1,2), (2,3)\} | F_i > 0\}$ all active surfaces. In our case, we can have at most three surfaces. However, it is important to note that we cannot have all three active surfaces around a load. Indeed, two of these surfaces (tension and compression) are independent and cannot be active at the same time. This leads us to 4 possible scenarios regardless of the coupling we have. The figure below explains the 4 scenarios we have for shear tension coupling. (the same scenarios are valid between compression and shear).

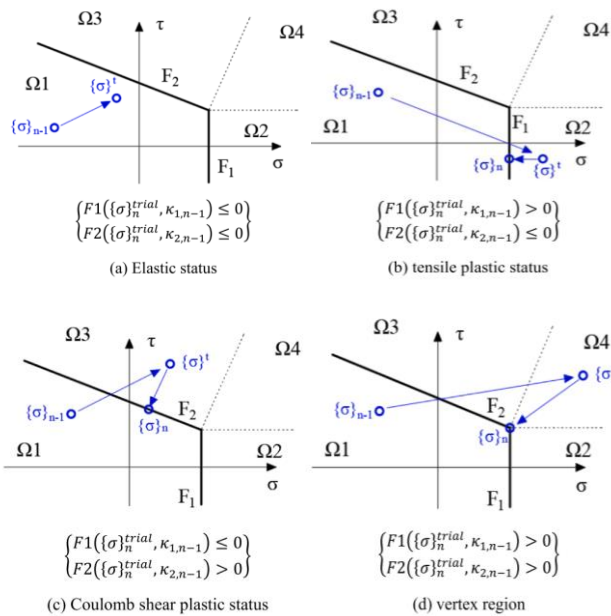


Figure 14 Possible scenario for the multi-surface radial return algorithm

2.5 Model algorigrams:

Once the behavior model is defined in the previous sections, the next step is to first implement this model at the Gaussian point scale for different load combinations to verify the robustness of our model. Subsequently, the model will be implemented in the *finite element software DIANA* to validate it on a structure.

To present the implementation steps of the previously defined model, we will use algorigrams summarizing the main steps of the digital implementation both at the local and global level. We will use the ISO 5807 rule to represent these algorigrams.

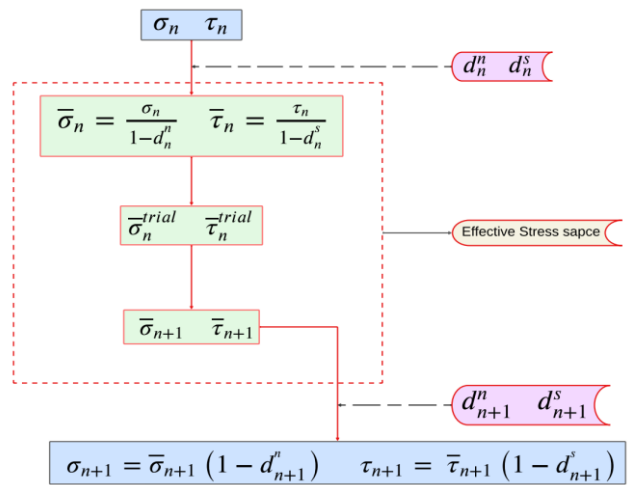


Figure 15 Algorigram of the transfer of nominal and effective stresses.

At the local level, we start by transferring the nominal stresses to the effective stresses before moving on to the radial return algorithm. Finally, the updated stresses will still be transferred to nominal stresses using the updated damage (Figure 15).

In the algorigram (Figure 15), the entire, red-framed part is made in the following algorigram. In the latter, the light blue steps are performed in the Newton-Raphson algorigram to solve the resulting nonlinear system. In the Newton-Raphson algorigram (Figure 17), We define an initial vector denoted X_0 grouping together all the unknowns of the problem (constraints and plastic multiplier). It is dimension 2, 3 or 4 depending on the position of the predicted stresses on the threshold surface.

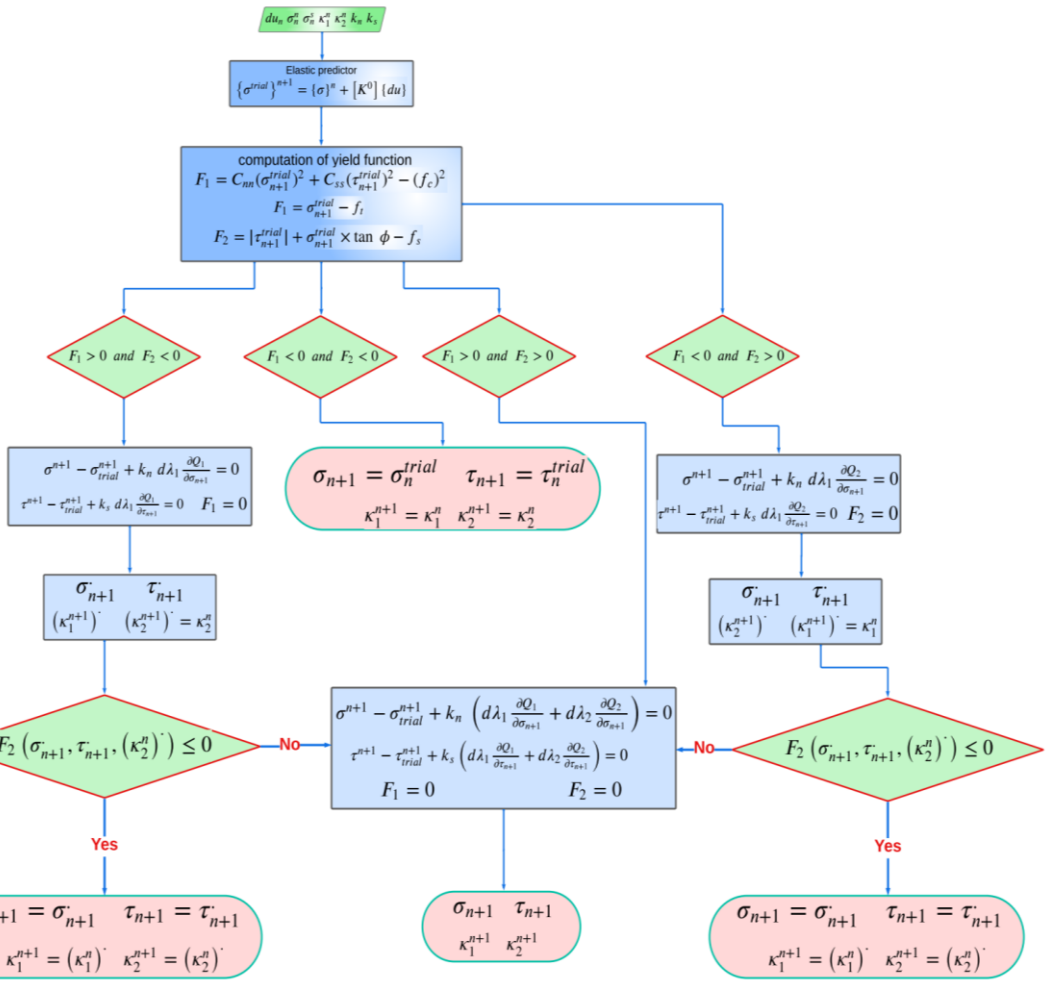


Figure 16 Algorigram of return-mapping in multi-surface plasticity.

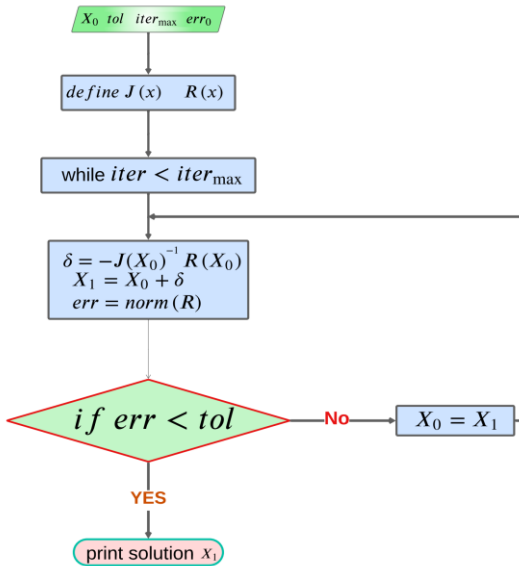


Figure 17 Newton Raphson algorigram

3 Finite elements and elastoplasticity with damage for masonry structure:

3.1 Introduction:

In this project, we will use the finite element method to simulate the overall behavior of masonry. As a

result, a mathematical description (called the constitutive law) of the behavior of materials giving the relationship between stress and strain (displacement) was developed in the previous section in the context of plasticity with damage.

From the assembly of the elements with the consideration of external forces and boundary conditions, the result is a system of equations describing the equilibrium of the structure that will be solved to obtain the displacements of the structure. From these displacements, we can then obtain the stresses and strains for each integration point.

The geometrical supports on which this model is built are interface elements: continuous elements with plane constraints and interface lines with zero thickness.

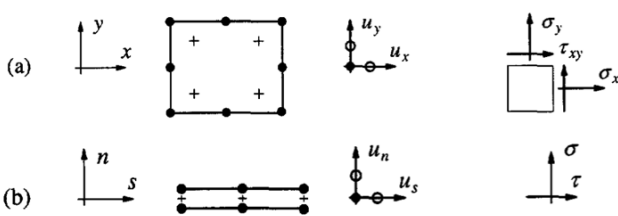


Figure 18 geometrical support for resolution in EF in 2D.

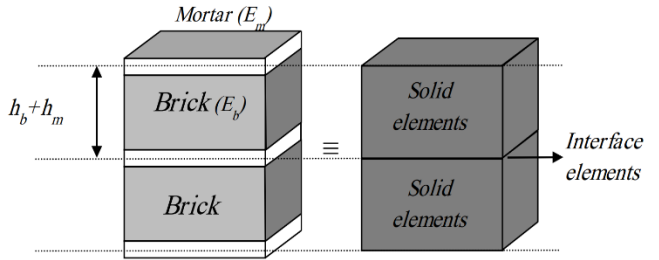


Figure 20 Detailed modeling and simplified modeling in 3D

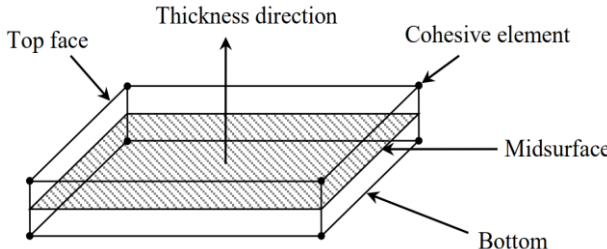


Figure 19 8-node finite element support for 3D modeling.

Among the modeling strategies to simulate the behavior of masonry, we will use the simplify method proposed by [6]. Bricks are extended to the thickness of the joints and are represented by continuous elements, while the behavior of the mortar of the joints and the interface is represented by a discontinuous element of zero thickness. The initial idea is to consider that damage propagates only along the weakest interface. This hypothesis is supported by numerous experimental observations and does not seem to significantly alter the global behavior at failure. This simplification is widely used for modeling masonry regardless of the calculation method used (FEM or DEM). However, when this simplification is implemented, the stiffness of the blocks and joints must be adapted to preserve the initial stiffness of the assembly. The behavior model is also written in the same way as before, with the stiffness terms depending on the mechanical and geometric properties of the masonry.

$$k_n = \frac{E_u E_m}{t_m(E_u - E_m)} \quad \text{and} \quad k_s = \frac{G_u G_m}{t_m(G_u - G_m)}$$

E_u and E_m are Young's modules and G_u and G_m are the shear moduli of the unit and the mortar respectively; t_m is the thickness of the joint.

3.2 Principle of FEM in Nonlinear Calculus:

Let's consider at a moment $t \in [0 ; T]$ an elastic body occupying a domain Ω border $\partial\Omega$ which is divided into $\partial\Omega_d$ subject to forced displacement, and $\partial\Omega_F$ subjected to imposed surface forces.

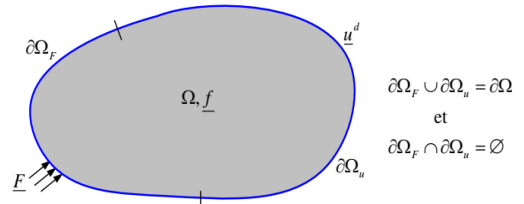


Figure 21 Solid Reference of Mechanical Problem

Mechanical resolution consists of always determining t the field of travel \mathbf{u} and constraints $\boldsymbol{\sigma}$ verifying the conditions:

- \mathbf{u} Kinematically admissible (C.A.) et $\mathbf{u} = \mathbf{u}_d$ sur $\partial\Omega_u$
- $\boldsymbol{\sigma}$ Statically admissible (S.A.): $\boldsymbol{\sigma}$ continuous, continuously differentiable and verifying:

$$\begin{cases} \operatorname{div} \boldsymbol{\sigma} + f = 0 & \text{on } \Omega \\ \boldsymbol{\sigma} \cdot \mathbf{n} = F & \text{on } \Omega_F \end{cases}$$

The application of the virtual work theorem to the system Ω Allows us to write to any virtual displacement field \mathbf{u}^* :

$$\int_{\Omega} \boldsymbol{\sigma} : \mathbf{E}(\mathbf{u}^*) d\Omega = \int_{\partial\Omega} F \cdot \mathbf{u}^* dS + \int_{\Omega} f \cdot \mathbf{u}^* d\Omega$$

The problem to be solved is non-linear. In this fact, we begin to discretize time (It should be noted here that this is a virtual time):

$$t_0 = 0, \quad t_1, \quad t_2, \dots, t_n, \quad t_{n+1}, \dots, t_M = T$$



Figure 22 Temporal discretization

Now suppose that we know the state of the structure now t_n ; we want to determine it over the interval $[t_n, t_{n+1}]$. A classic assumption is that the history of displacement is linear over the time interval $[t_n, t_{n+1}]$ that is:

$$u(\tau) = \frac{t_{n+1} - \tau}{\Delta t} u_n + \frac{\tau - t_n}{\Delta t} u_n$$

$$\tau \in [t_n, t_{n+1}] \quad \text{and} \quad \Delta t = t_{n+1} - t_n$$

The problem then is to find the macroscopic fields σ, u, E verifying the CA and SA conditions stated above. To solve the incremental problem by the finite element method, the domain is classically subdivided Ω into a finite number of elements. On each element, the displacement field is determined from the node displacements U ou (U^*) by:

$$\{u\} = [N]\{U\} \quad \{u^*\} = [N]\{U^*\}$$

$[N]$ Represents the matrix of interpolation functions. Similarly, the deformation field can be written from the deformation matrix $[B]$

$$\{E\} = [B]\{U\} \quad \{E^*\} = [B]\{U^*\}$$

By relating these equations in the principle of virtual work, we obtain:

$$\int_{\Omega} [U^*]^T [B]^T \{\sigma\} d\Omega = \int_S [U^*]^T [N]^T [F] dS + \int_{\Omega} [U^*]^T [B]^T \{f\} d\Omega$$

This equation must be always true for all $[U^*]$ C.A. It follows that the fields must satisfy the instantaneous t_{n+1} :

$$\underbrace{\int_{\Omega} [B]^T \{\sigma_{n+1}\} d\Omega}_{F_{int}} = \underbrace{\int_S [N]^T [F_{n+1}] dS}_{F_{ext}} + \underbrace{\int_{\Omega} [N]^T \{f_{n+1}\} d\Omega}_{F_{ext}}$$

$$\Rightarrow F_{int} - F_{ext} = \{R(U_{n+1})\} = 0$$

F_{ext} And F_{int} are respectively the intern and extern forces of the structure. $R(U_{n+1})$ Represents the residual forces at each load increment should tend green 0

3.3 Solving Equations and Iterative Schema:

Since the problem we are trying to solve is nonlinear due to material nonlinearity, it is necessary to adapt an iterative approach to solve it (in our case, the Newton Raphson method). There is an implicit approach.

Suppose that at the beginning of the iteration i We have an approximation U_{n+1}^i of the solution such that the residual forces are not zero $\{R(U_{n+1})\} \neq 0$. A correction is then sought δU_{n+1}^{i+1} Nodal shifts verifying: $\{R(U_{n+1} + \delta U_{n+1}^{i+1})\} = 0$. By performing a first-order linearization of the residual forces, we obtain:

$$\begin{aligned} \{R(U_{n+1} + \delta U_{n+1}^{i+1})\} \\ = \{R(U_{n+1}^i)\} + \mathbb{K}(U_{n+1}^i) \delta U_{n+1}^{i+1} \end{aligned}$$

With $\mathbb{K}(U_{n+1}^i)$ The tangent stiffness matrix determined by the expression:

$$\mathbb{K}(U_{n+1}^i) = \frac{\partial R(U_{n+1}^i)}{\partial U_{n+1}^i} = \int_{\Omega} [B]^T [\mathbb{L}_{n+1}^i] [B] d\Omega$$

$[\mathbb{L}_{n+1}^i]$ Represents the tangent operator of the local behavior law, and it is given by:

$$[\mathbb{L}_{n+1}^i] = \frac{\partial \sigma_{n+1}^i}{\partial du_{n+1}^i}$$

It follows, therefore, $U_{n+1}^{i+1} = U_{n+1}^i + \delta U_{n+1}^{i+1}$.

In the next chapter, we will give the steps of numerical implementation in the form of an algorigram on a global scale.

3.4 Determining the Consistent Tangent Operator (CTO):

As we saw in the previous section, the global solution of the system requires the determination of the global tangent matrix of stiffness, which in turn is related to the local tangent operator. This operator is related to the constitutive law that we constructed above.

$$[\mathbb{L}_{n+1}^i] = \frac{\partial \{\sigma_{n+1}^i\}}{\partial \{du_{n+1}^i\}}$$

We have: $\sigma_{n+1}^i = ([I] - [D])\{\bar{\sigma}_{n+1}\} \Rightarrow$

$$[\mathbb{L}_{n+1}^i] = ([I] - [D]) \frac{\partial \{\bar{\sigma}_{n+1}\}}{\partial \{du_{n+1}^i\}} - \{\bar{\sigma}_{n+1}^i\} \left(\frac{\partial [D]^{n+1}}{\partial \{du_{n+1}^i\}} \right)^T$$

Where $\frac{\partial \{\bar{\sigma}_{n+1}\}}{\partial \{du_{n+1}^i\}}$ can be regarded as the CTO of the plasticity component of the model expressed in terms of effective stress space $\{\bar{\sigma}_{n+1}\}$. This can be derived by the following expressions:

$$\begin{aligned} \frac{\partial}{\partial \{du_{n+1}^i\}} & \left[\{\bar{\sigma}_{n+1}\} + \lambda^{n+1}[K] \frac{\partial Q}{\partial \{\bar{\sigma}_{n+1}^i\}} \right] \\ & F_i(\{\bar{\sigma}_{n+1}^i\}) \\ = \frac{\partial}{\partial \{du_{n+1}^i\}} & \left[\{\bar{\sigma}_n\} + [K]\{du_{n+1}^i\} \right] \end{aligned}$$

The derivative of the left-hand side of the above equation is expressed in term of $\bar{\sigma}_{n+1}^i$ and λ^{n+1} using chain

$$\frac{\partial}{\partial (\{\bar{\sigma}_{n+1}^i\}, \lambda^{n+1})} \left[\begin{array}{c} \{\bar{\sigma}_{n+1}\} + \lambda^{n+1}[K] \frac{\partial Q}{\partial \{\bar{\sigma}_{n+1}^i\}} \\ F_i(\{\bar{\sigma}_{n+1}^i\}) \end{array} \right] \frac{\partial (\{\bar{\sigma}_{n+1}^i\}, \lambda^{n+1})}{\partial \{du_{n+1}^i\}} = [J]^{n+1} \begin{bmatrix} \frac{\partial \{\bar{\sigma}_{n+1}\}}{\partial \{du_{n+1}^i\}} \\ \frac{\partial \lambda^{n+1}}{\partial \{du_{n+1}^i\}} \end{bmatrix} = \begin{bmatrix} [K] \\ [0] \end{bmatrix}$$

From this above expression, the CTO for the plasticity component is written using a projection matrix $[P]$ by the following expression:

$$\frac{\partial \{\bar{\sigma}_{n+1}\}}{\partial \{du_{n+1}^i\}} = [P]^T ([J]^{n+1})^{-1} [P] [K]$$

The size of the projection matrix is adapted following the scenario that we have i.e. the size of the Jacobian matrix.

- For uniaxial tension $[P]^T = \begin{bmatrix} 1 & 0 \\ 0 & 1 \end{bmatrix}$
- For uniaxial shear or compression:

$$[P]^T = \begin{bmatrix} 1 & 0 & 0 \\ 0 & 1 & 0 \end{bmatrix}$$

- For coupling scenario (shear and tension or shear and compression):

$$[P]^T = \begin{bmatrix} 1 & 0 & 0 & 0 \\ 0 & 1 & 0 & 0 \end{bmatrix}$$

The derivative of the damage parameter with respect to the increment of displacement $\frac{\partial [D]^{n+1}}{\partial \{du_{n+1}^i\}}$ is expressed using the chain rule in the following form:

$$\frac{\partial [D]^{n+1}}{\partial \{du_{n+1}^i\}} = \frac{\partial [D]^{n+1}}{\partial \dot{\kappa}_{n+1}} \frac{\partial \dot{\kappa}_{n+1}}{\partial \lambda^{n+1}} \frac{\partial \lambda^{n+1}}{\partial \{du_{n+1}^i\}}$$

As we seen previously, the last part of this equation is: $\frac{\partial \lambda^{n+1}}{\partial \{du_{n+1}^i\}} = [0]$. At the end we can have:

$$[\mathbb{L}_{n+1}^i] = ([I] - [D]) [P]^T ([J]^{n+1})^{-1} [P] [K]$$

3.5 Numerical implementation at the global level:

The finite element software DIANA, used for the numerical simulations in this project, offers a key feature:

rule, while the right-hand side will retain elastic stiffness $[K]$ only as $\{\bar{\sigma}_n\}$ is constant at current time step. We will also use the relation of the derivative of Jacobian as developed previously in to have a compact relation.

it allows the introduction of custom behavior laws through a user subroutine called USRIFC. This subroutine, designed primarily for interfaces, enables the updating of the tensile vector, internal variables, and tangent stiffness matrix. The behavior model we have developed will be adapted to meet DIANA's required format, with the model parameters provided in [7.4](#). As explained in the finite element section, the problem will be solved at both the global and local levels. Newton-Raphson's algorithm will be employed at each level to ensure the structure's local and global equilibrium. The algorigram in [Figure 25](#) outlines the calculation steps for solving the overall problem, with the yellow section representing processes at the local scale (corresponding to the set of algorigrams previously established).

4 Model validation:

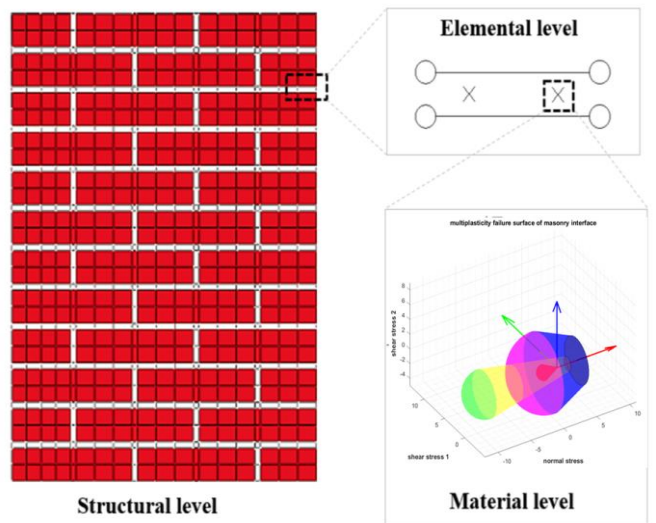


Figure 23 step of model validation

To ensure the robustness of the model developed above, we must validate it at 3 levels (Gaussian point, material, structure) according to the diagram below

4.1 Gauss point validation:

In this validation, we present the variations of the threshold area during the loading phases for simple tests.

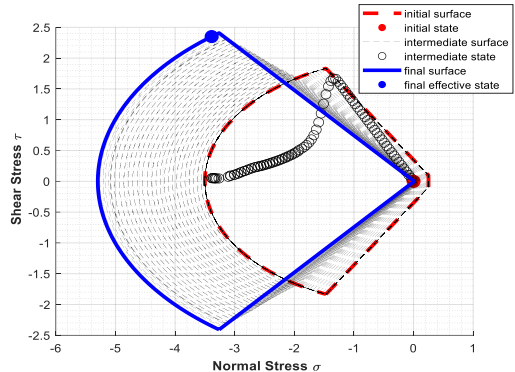


Figure 24 Proportional Compression/Shear Loading

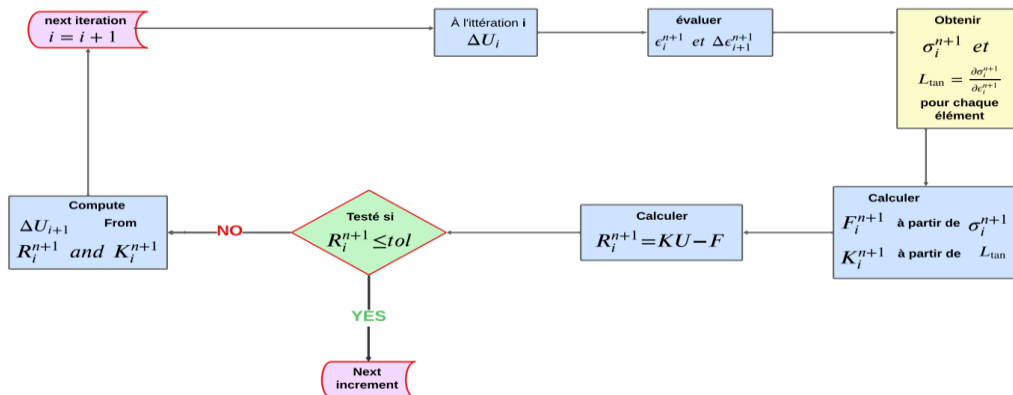


Figure 25 algorigram of the model at the global scale

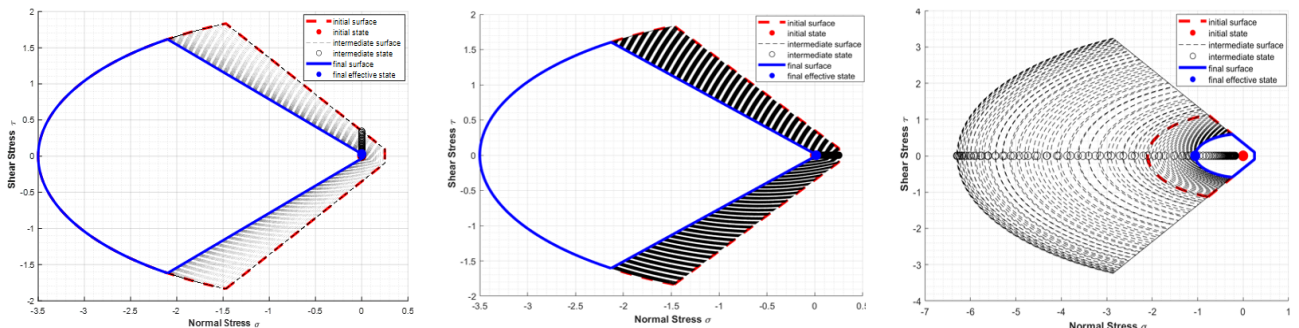


Figure 26 Elementary result uniaxial shear (a) tension (b) and compression (c)

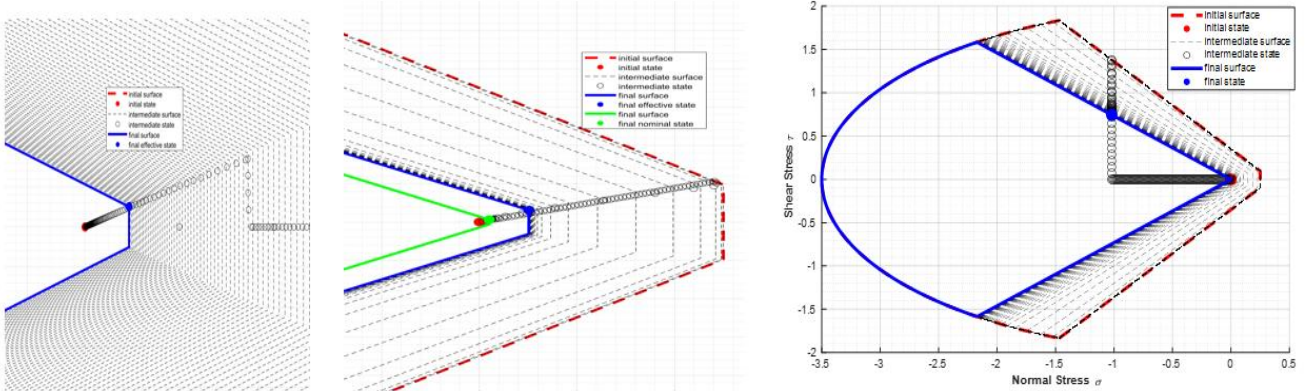


Figure 27 tension + shear proportional (a) tension + shear non-proportional (b) compression + shear non-proportional (c)

On the above elastic surfaces, we see an effect at the tensile and shear loading levels of a link between the two stresses. In fact, the surface made up of these two parts varies simultaneously according to the same

ratio, which is the damage. However, in the tension and compression load, it can be noted that the slope of the Mohr Coulomb line does not change, which indicates a non-correlation between the two solicitations.

4.2 Material validation:

In the next section, we will perform several fundamental tests that we developed earlier on the behavior of the interface with simple configurations. We consider a simplified model. The dimension of bricks in the

simplified state is $200 \times 100 \times 50 \text{ mm}^3$. We also consider a mesh made up of a single element. We recall that bricks have an isotropic linear behavior and that only interfaces are subject to nonlinearities.

Tension		Shear				Compression			
f_t	G_f^I	c	G_f^{II}	$\tan \psi$	$\tan \phi_i$	$\tan \phi_r$	f_c	G_{fc}	C_{ss}
0,25	0,010	0,35	0,125	0,05	1,01	0,46	6,3	5,5	9

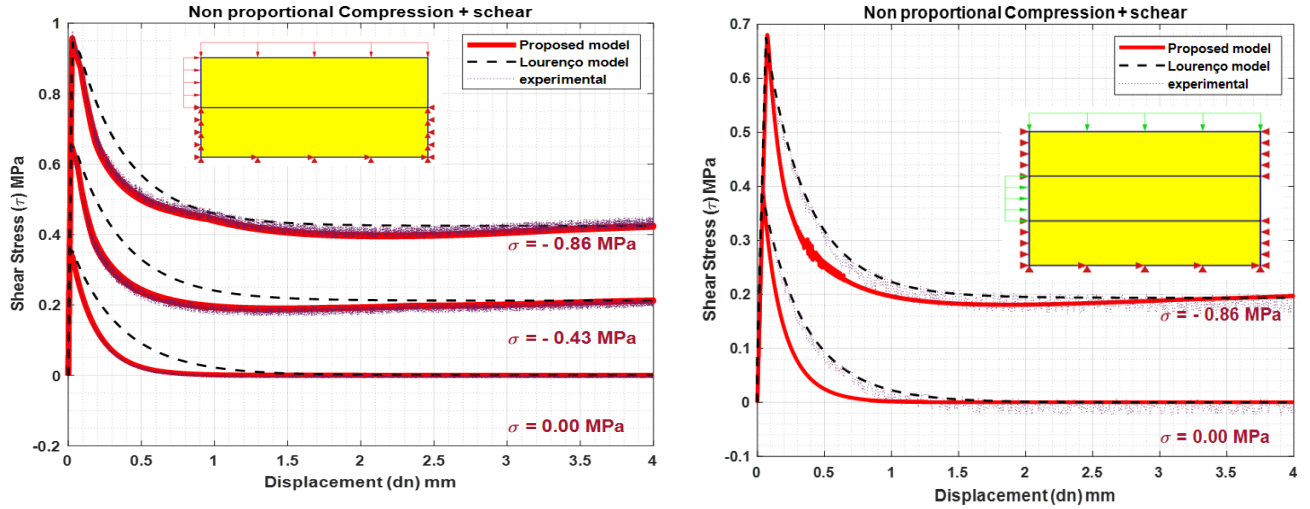


Figure 28 shear test with non-proportional pre-compression couplet (a) and triplet (b)

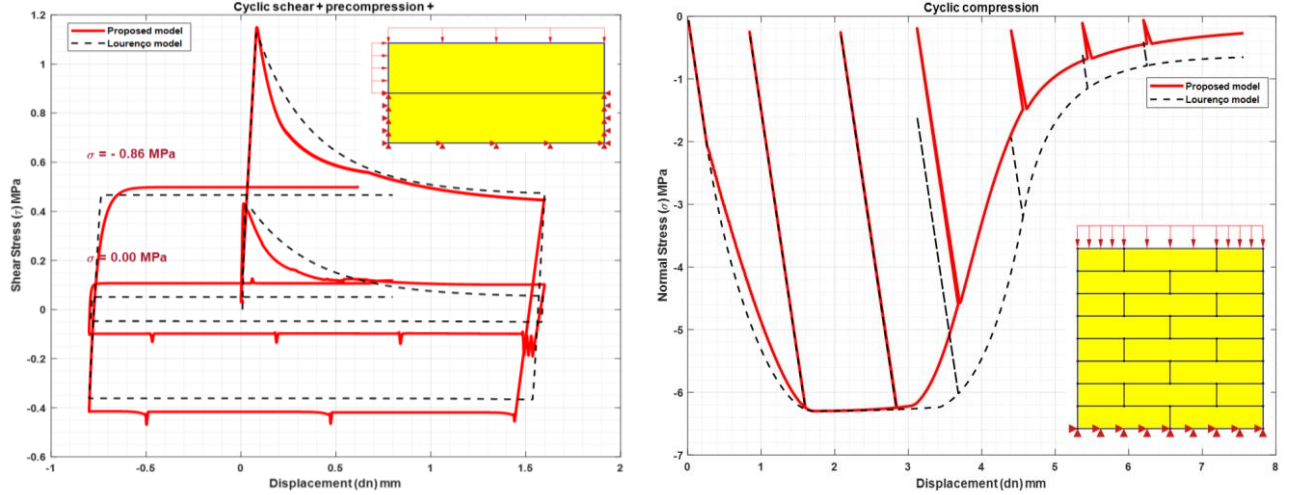
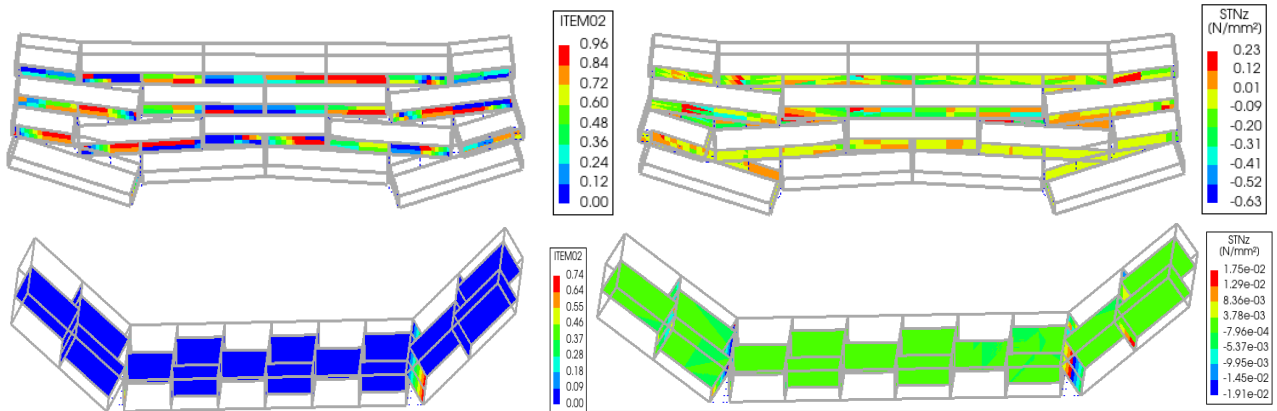


Figure 29 Cyclic shear tests with pre-compression (a) and cyclic compression (b)



Interface Damage profile

stress damage profile

Figure 30 Deformation profile of in-plane and out-of-plane cyclic bending tests

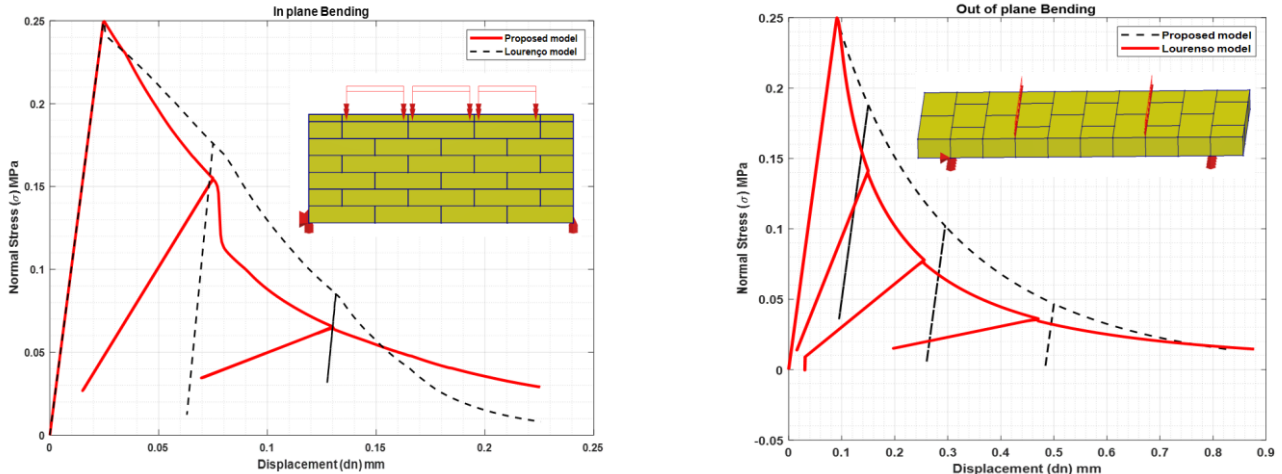


Figure 31 Cyclic bending tests in the plane (a) out of the plane (b)

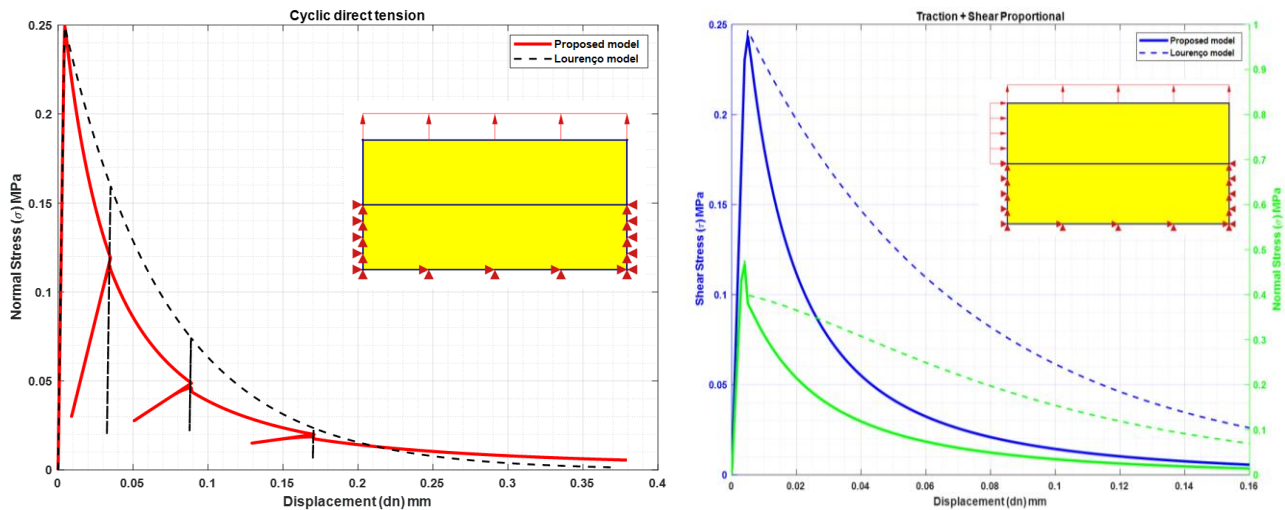


Figure 32 Direct Cyclic Tensile (a) and Tensile + Proportional Shear (b) Tests

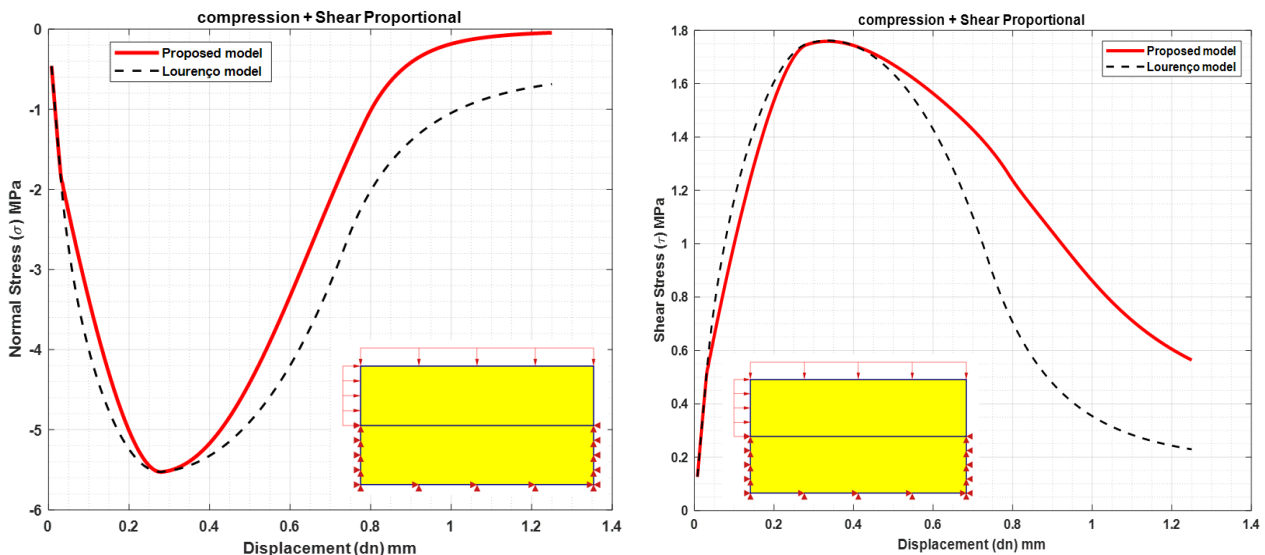


Figure 33 compression tests + proportional shear on couplet

All the tests at the material scale above give us good results of the behavior we wished. However, in the non-proportional shear tests with pre-compression, we

observed convergence difficulties which resulted in the presence of some noise due to the instability of the solver used. However, the curves follow an acceptable

pace despite these noises. The difference observed between our model and Lourenço's model is mainly due to the wording of ours. We formulated our model in an elastoplastic frame with damage and we integrated a secant discharge in the tensile behavior which is the one generally observed in the experimental results.

4.3 Structural Validation:

Both COMP_3 and COMP_6 are quasi-static cyclical tests conducted at the Technical University of Delft.

COMP_3 features a wall sample measuring 1.1 m wide, 2.76 m high, and 102 mm thick, subjected to an overburden stress of 0.4 MPa under double-clamped boundary conditions. The test involves an initial vertical load on the top left face and the wall's dead weight, followed by horizontal displacements to apply cyclic loads with increasing amplitudes from 1 mm to 35 mm.

COMP_6 involves a larger wall sample, 4.0 m wide, 2.76 m high, and 102 mm thick, with a pre-compression of 0.5 MPa, tested under cantilevered boundary conditions. A rigid beam ensures these conditions, and vertical loading is applied along the top edge, along with the dead weight. After these initial steps, cyclic loads are applied with increasing amplitudes ranging from 0.25 mm to 15.6 mm. The new constitutive model with 10 parameters is used for the interface elements in this test.

In the first steps, the vertically distributed load is applied along the top edge. The dead weight of the wall is also applied in these five steps. After the first five steps, a series of prescribed horizontal displacements are applied to achieve a cyclic load with increasing cycle amplitudes.

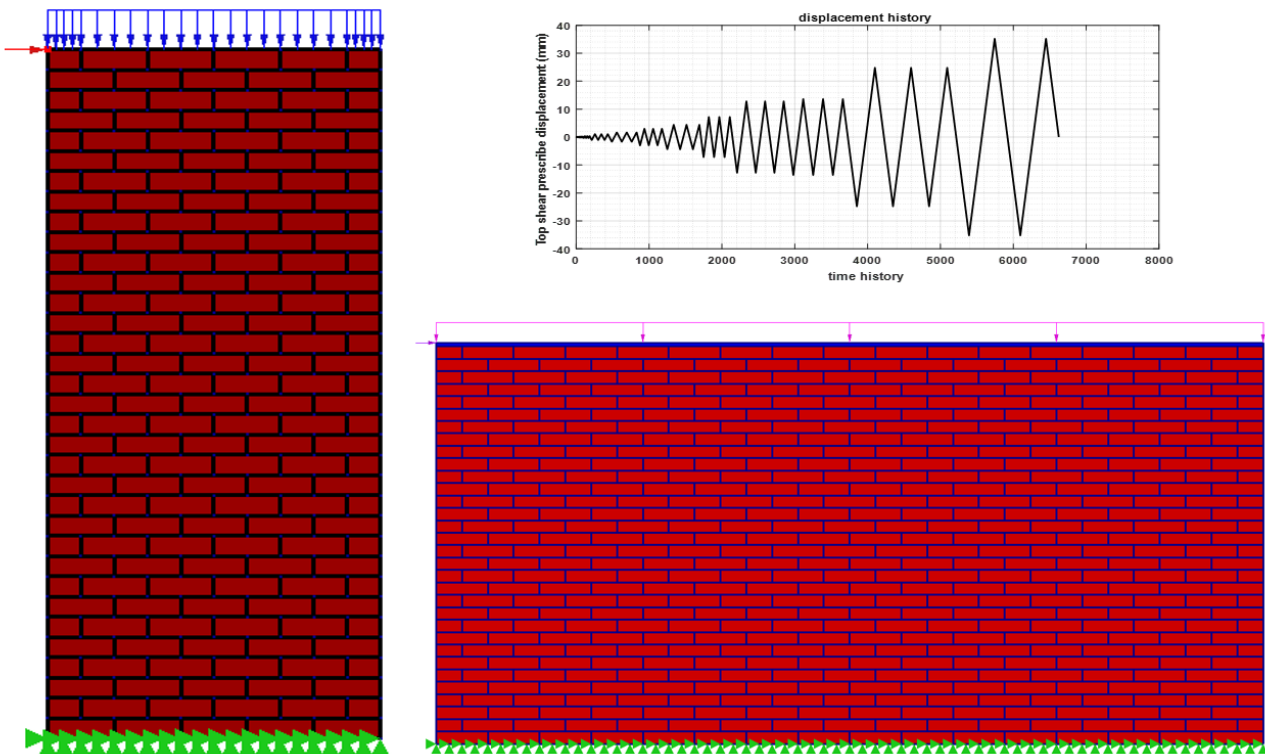


Figure 34 Geometry of wall for analysis (a) TUD COMP3 (b) TUD COMP 6 (c) load history

4.3.1 Flexural failure (Double-fixed Wall Test comp_3):

In the non-calibrated model, the observed behavior shows significant divergences from the experimental results. Notably, the absence of crushing at the heel of

the wall keeps the contact area very small, even when the wall is almost fully unloaded, which contrasts with the real behavior where the contact area is larger due

to mortar crushing and brick cracking. This discrepancy is attributed to the assumption of fully elastic behavior of the bricks in the analysis, thereby underestimating plastic deformation. Additionally, the force-displacement curve (**Figure 36 a**) shows that for cycles with large lateral displacement, the structure unloads with little reduction in shear force, exhibiting typical rocking behavior with minimal toe crushing. Consequently, the contact area for compression in the bottom mortar layer is very small, allowing the peak shear force to be analytically calculated by considering moment equilibrium.

To address this, the model was calibrated by reducing the compressive strength of the bed joint to 2 MPa and the compression fracture energy to 12.85 N/mm, to keep the area under the softening curve unchanged.

These adjustments allowed for a better reproduction of

the experimentally observed behavior, and the re-started analysis showed improved alignment between the numerical model and the experimental results. Compared to the absolute value of the relative interface displacement in the non-calibrated model, the calibrated model (**Figure 35**) shows greater deformation at the toe. This is further supported by the relative normal displacement of the bed joint, which has a maximum compression displacement of 7.27 mm. This value is reasonable, as it is lower than the actual thickness of the mortar layer (10 mm) observed in the experiment. The tensile crack width at the opposite end of the bed joint is like that of the non-calibrated model, with a maximum value of 3.38 mm. Overall, the failure mode closely mirrors the experimental result, characterized by flexural failure with some toe crushing.

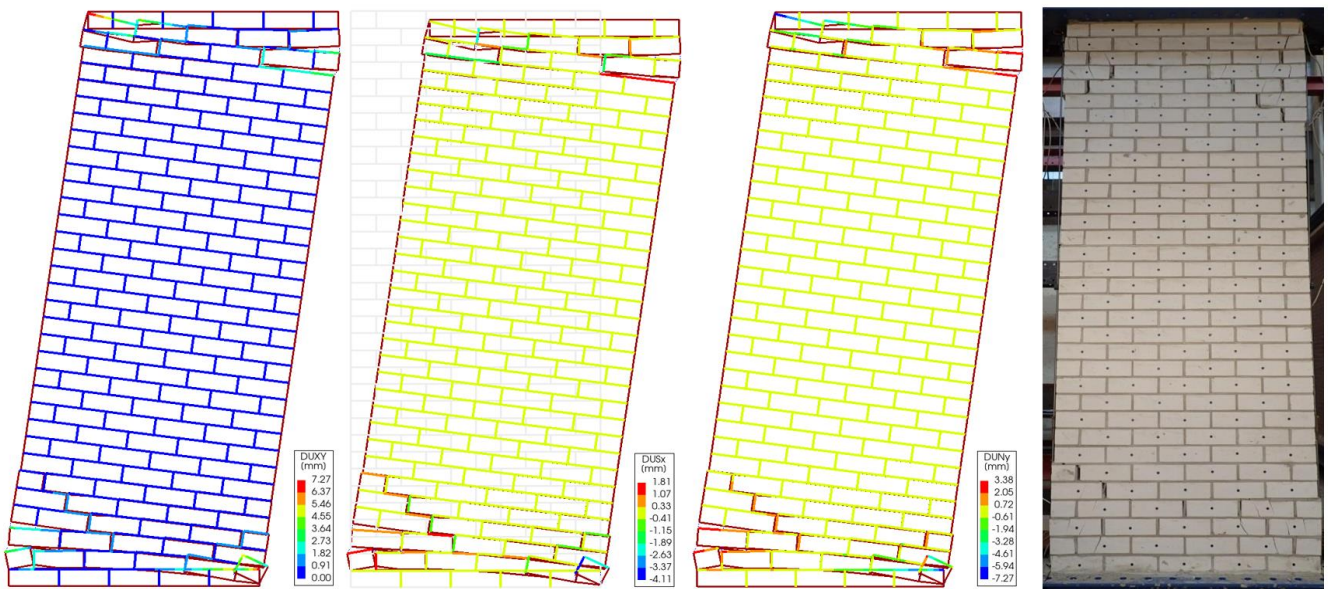


Figure 35 wall cracking profile for the calibrated model TUD COP_3 with 35 mm loading (a) absolute displacement (b) relative shear displacement (c) and normal displacement (d) experimental

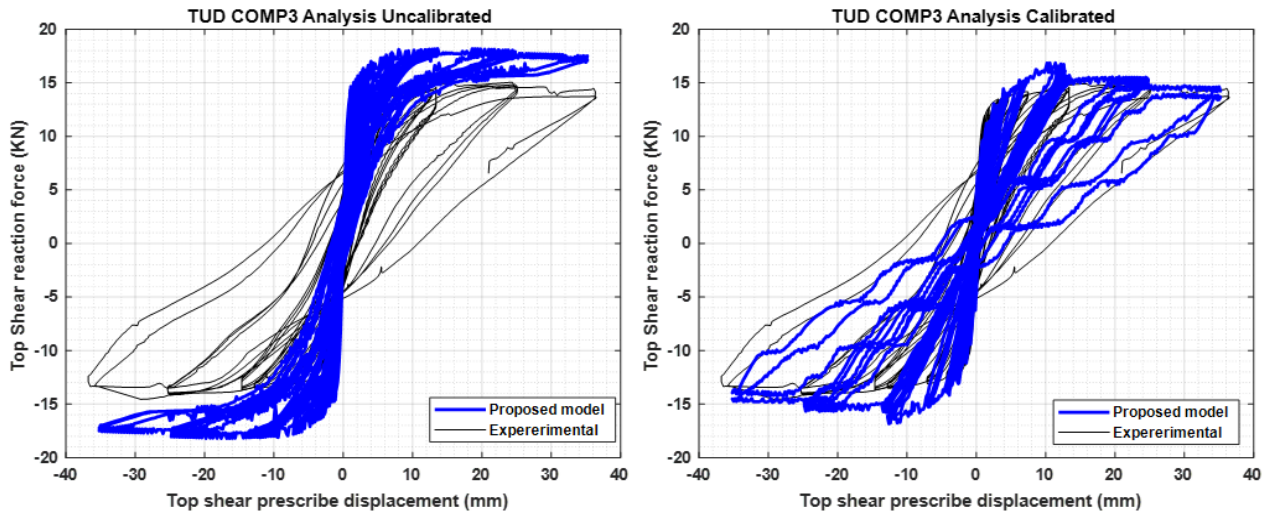


Figure 36 Top Prescribed Shear Displacement (mm)

For the calibrated model, the force-displacement curve (**Figure 36 b**) shows very good agreement with the experimental results in terms of initial stiffness, unloading stiffness at the end of loading, and energy dissipation. The ultimate shear capacity is slightly higher than the experiment but remains satisfactory. The shear capacity of the wall gradually decreases over the cycles, reaching the shear force observed in the experiment during the final cycle. Moreover, the last two unloading events in the negative direction show some fluctuation, which could be smoothed with mesh refinement of the bed joints. The degradation within each cycle for multiple loadings closely matches the experimental results, especially during the final cycle. Therefore, this calibrated analysis demonstrates good consistency with the experimental data.

4.3.2 Combined Shear and Bending Failure (Can-tilever test COMP_6)

The numerical analysis (**Figure 37**) shows diagonal staircase cracks similar to those observed in the

experiment, but with differences in the location of the crack intersections: in the analysis, they intersect at the bottom of the wall, while in the experiment, they are located at the upper left. The numerical model highlights a shear sliding failure, unlike the experiment, where flexural failure and corner crushing reduce the wall's capacity.

The force-displacement curves (**Figure 40 a**) show that, although the initial stiffness and loading capacity are accurate, the analysis overestimates energy dissipation and unloading stiffness. This discrepancy is due to increased shear sliding, whereas the experiment reveals flexural restoration due to corner crushing. To address this, the friction angle was increased from 23.27° to 26.57° , and the compressive strength was reduced from 5.98 MPa to 4 MPa. These adjustments improved the match, and further reducing the strength to 3 MPa or 2 MPa could better align the results with the experiment by promoting more corner crushing.

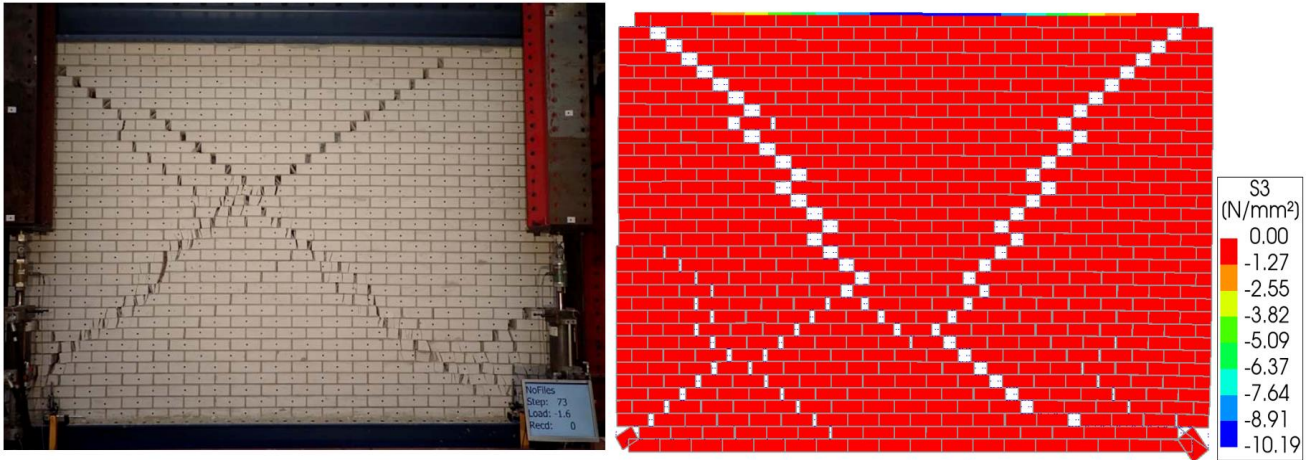


Figure 37 Crack pattern on the TUD wall COMP_6 Experimental VS Uncalibrated Numerical Analysis

The calibrated analysis (**Figure 39 a and b**) shows significant improvements over the un-calibrated model, particularly with notable toe crushing at the bottom mortar layer and a reduction in maximum shear displacement to 23.53 mm. The staircase cracks are now more concentrated in the upper part of the wall,

reflecting a better match with the experiment, though the crack pattern remains more symmetric in the analysis. Despite the remaining discrepancies in the crack pattern, the calibrated model better replicates the combination of shear cracking and toe crushing observed in the experiment.

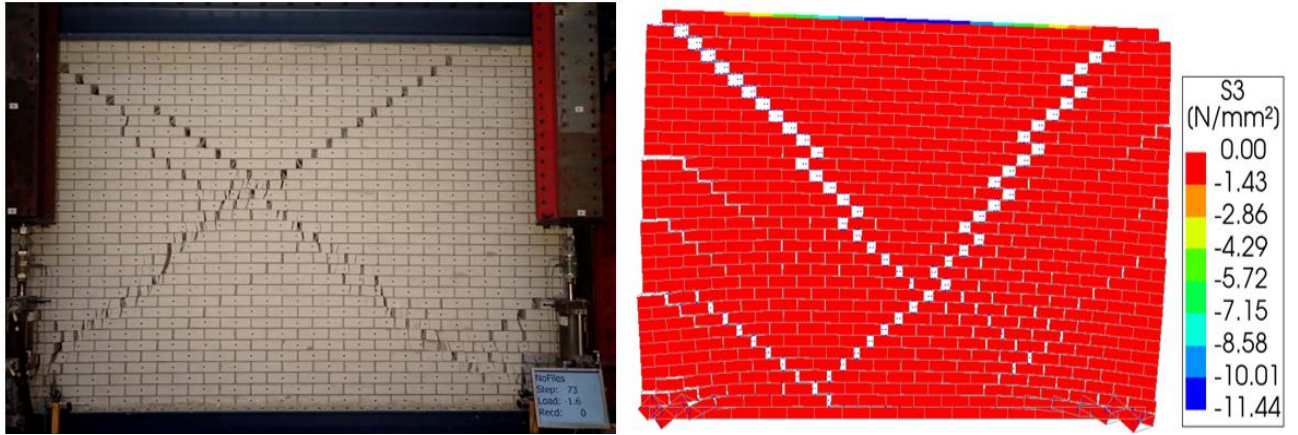


Figure 38 Crack pattern on the TUD wall COMP_6 Experimental VS Uncalibrated Numerical Analysis

The calibrated model's force-displacement curve (**Figure 40 b**) closely matches the experimental results, particularly in terms of initial stiffness, ultimate capacity, unloading stiffness, and energy dissipation. The main difference is that peak capacity degradation occurs one cycle later in the analysis compared to the experiment. Both the experiment and the analysis show a transition from combined shear and flexural behavior to flexural-

dominated failure as loading progresses. The degradation within a cycle is linked to a reduction in shear capacity and a shrinkage of the loop area, primarily due to toe crushing. However, in the experiment, toe crushing is characterized by brick splitting, while in the analysis, it occurs as bed joint crushing. Overall, the calibrated analysis effectively replicates the experimental outcomes.

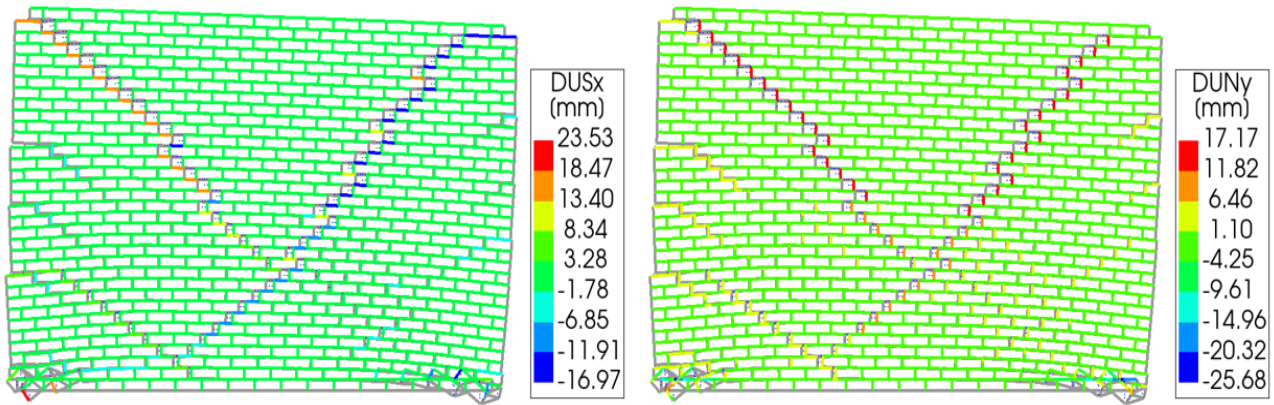


Figure 39 wall cracking profile TUD COP_6 with 15.5 mm loading (a) relative shear displacement (b) normal relative displacement uncalibrated model

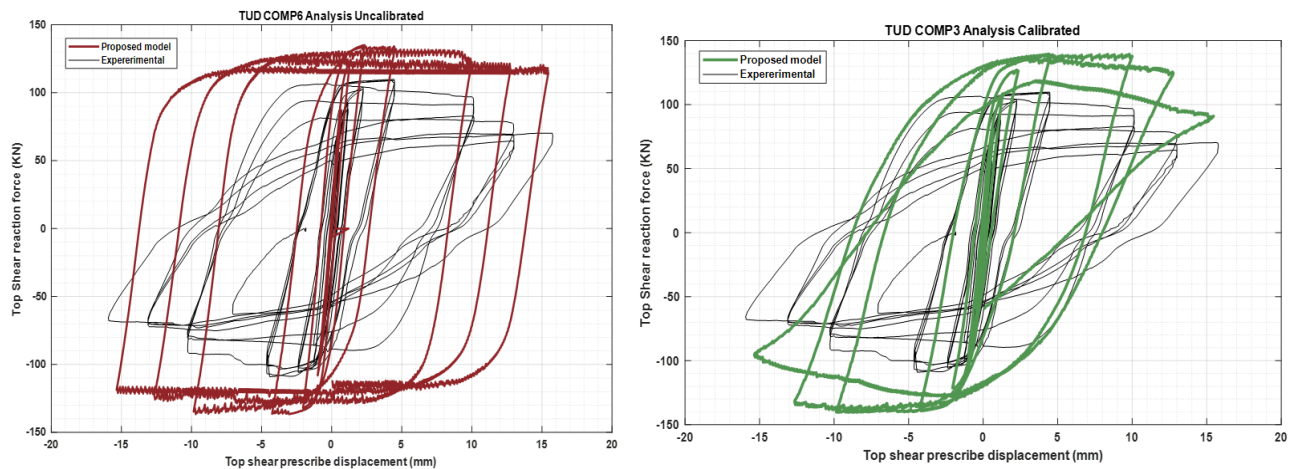


Figure 40 Top Shear Prescribed Displacement (mm)

5 Conclusion:

In this project, we developed a robust and reliable model for simulating the behavior of masonry wall joints under both in-plane and out-of-plane monotonic and cyclic loads. Implemented in the DIANA finite element software via a custom subroutine, our model integrates a damage framework within multi-surface plasticity and incorporates secant unloading in tension. This bi-dimensional and tri-dimensional model is formulated in the effective stress space, enhancing robustness by preventing yield surface softening and improving convergence stability.

The numerical implementation employs a fully implicit backward Euler integration technique, ensuring high accuracy and robustness in the iterative Newton-Raphson process. An adaptive sub-stepping method further enhances numerical stability and efficiency by

dynamically adjusting the load increment size based on previous iterations' performance.

Our model's performance was validated through finite element analysis of masonry structures at various scales and loading scenarios, including monotonic and cyclic tension, compression, and shear tests on masonry specimens, as well as in-plane and out-of-plane loads on masonry panels and walls. Extensive experimental validation against benchmark tests from the literature demonstrated the model's high accuracy, robustness, and computational efficiency, making a significant contribution to the field of masonry structural analysis.

6 References:

- [1] J. Vaculik, « Unreinforced masonry walls subjected to out-of-plane seismic actions ».
- [2] N. Mendes et P. Lourenco, « Seismic Vulnerability of Existing Masonry Buildings: Nonlinear

- Parametric Analysis », 2015, p. 139-164. doi: 10.1007/978-3-319-16130-3_6.
- [3] P. B. Lourenço, « Computations on historic masonry structures », *Progress in Structural Engineering and Materials*, vol. 4, n° 3, p. 301-319, 2002, doi: 10.1002/pse.120.
- [4] O. Omidi et V. Lotfi, « Finite Element Analysis of Concrete Structures Using Plastic-Damage Model in 3-D Implementation », *International Journal of Civil Engineering*, vol. 8, p. 187-203, sept. 2010.
- [5] J. Zhang, Z. Zhang, et C. Chen, « Yield Criterion in Plastic-Damage Models for Concrete », *Acta Mechanica Solida Sinica*, vol. 23, n° 3, p. 220-230, janv. 2010, doi: 10.1016/S0894-9166(10)60024-9.
- [6] P. B. Lourenco, « Computational strategies for masonry structures », 1996, Consulté le: 10 octobre 2023. [En ligne]. Disponible sur: <https://repository.tudelft.nl/islandora/object/uuid%3A4f5a2c6c-d5b7-4043-9d06-8c0b7b9f1f6f>
- [7] L. Facconi, F. Minelli, et F. Vecchio, *Predicting Uniaxial Cyclic Compressive Behavior of Brick Masonry: New Analytical Model*, vol. 144. 2017. doi: 10.1061/(ASCE)ST.1943-541X.0001961.
- [8] L. Macorini et B. A. Izzuddin, « A non-linear interface element for 3D mesoscale analysis of brick-masonry structures », *International Journal for Numerical Methods in Engineering*, vol. 85, n° 12, p. 1584-1608, 2011, doi: 10.1002/nme.3046.
- [9] Y. Oktiovan, F. Messali, B. Pulatsu, J. Lemos, et J. Rots, « A contact-based constitutive model for the numerical analysis of masonry structures using the distinct element method », *Computers & Structures*, vol. 303, p. 107499, août 2024, doi: 10.1016/j.compstruc.2024.107499.
- [10] J. Lemos, « Discrete Element Modeling of Masonry Structures », *International Journal of Architectural Heritage - INT J ARCHIT HERIT*, vol. 1, p. 190-213, mai 2007, doi: 10.1080/15583050601176868.
- [11] P. A. Cundall et O. D. L. Strack, « A discrete numerical model for granular assemblies », *Géotechnique*, vol. 29, n° 1, p. 47-65, mars 1979, doi: 10.1680/geot.1979.29.1.47.
- [12] A. M. D'Altri et al., « Modeling Strategies for the Computational Analysis of Unreinforced Masonry Structures: Review and Classification », *Arch Computat Methods Eng*, vol. 27, n° 4, p. 1153-1185, sept. 2020, doi: 10.1007/s11831-019-09351-x.
- [13] G. Alfano et E. Sacco, « Combining interface damage and friction in cohesive-zone model », *International Journal for Numerical Methods in Engineering*, vol. 68, p. 542-582, oct. 2006, doi: 10.1002/nme.1728.
- [14] A. D'Altri, F. Messali, J. Rots, G. Castellazzi, et S. Miranda, « A damaging block-based model for the analysis of the cyclic behaviour of full-scale masonry structures », *Engineering Fracture Mechanics*, vol. 209, p. 423-448, févr. 2019, doi: 10.1016/j.engfracmech.2018.11.046.
- [15] Y. Nie, T. Xie, G. Chen, X.-Y. Zhao, et J.-B. Lv, « A 2D generic multi-surface cohesive zone model for simulating FRP-to-concrete mixed-mode debonding failure », *Composite Structures*, vol. 296, p. 115890, sept. 2022, doi: 10.1016/j.compstruct.2022.115890.
- [16] A. M. D'Altri, S. De Miranda, G. Castellazzi, et V. Sarhosis, « A 3D detailed micro-model for the in-plane and out-of-plane numerical analysis of masonry panels », *Computers & Structures*, vol. 206, p. 18-30, août 2018, doi: 10.1016/j.compstruc.2018.06.007.
- [17] A. Page, « Finite element model for masonry », *ASCE J Struct Div*, vol. 104, p. 1267-1285, août 1978, doi: 10.1061/JSDEAG.0005406.
- [18] P. Kumar, A. Rajagopal, et M. Pandey, « Plasticity based interface model for failure modelling of unreinforced masonry under cyclic loading », *Vietnam Journal of Mechanics*, vol. 42, p. 1-18, sept. 2020, doi: 10.15625/0866-7136/15479.
- [19] « 60-Yu-Nie.pdf ». Consulté le: 1 septembre 2024. [En ligne]. Disponible sur: <https://aees.org.au/wp-content/uploads/2019/12/60-Yu-Nie.pdf>
- [20] L. Gambarotta et S. Lagomarsino, « Damage models for the seismic response of brick masonry shear walls. Part I: The mortar joint model and its applications », *Earthquake Engineering & Structural Dynamics*, vol. 26, p. 423-439, avr. 1997, doi: 10.1002/(SICI)1096-9845(199704)26:4<423::AID-EQE650>3.0.CO;2-#.
- [21] Y. Nie, A. Sheikh, P. Visintin, et M. Griffith, « A robust computational strategy for failure prediction of masonry structures using an improved multi-surface damage-plastic based interface model », *International Journal for Numerical Methods in Engineering*, vol. 124, n° 11, p. 2498-2528, 2023, doi: 10.1002/nme.7218.
- [22] Y. Nie, A. Sheikh, P. Visintin, et M. Griffith, « An interfacial damage-plastic model for the simulation of masonry structures under monotonic and cyclic loadings », *Engineering Fracture Mechanics*, vol. 271, p. 108645, août 2022, doi: 10.1016/j.engfracmech.2022.108645.

- [23] A. Spada, G. Giambanco, et P. Rizzo, « Damage and plasticity at the interfaces in composite materials and structures », *Computer Methods in Applied Mechanics and Engineering*, vol. 198, p. 3884-3901, nov. 2009, doi: 10.1016/j.cma.2009.08.024.
- [24] Y. Nie, A. Sheikh, M. Griffith, et P. Visintin, « A damage-plasticity based interface model for simulating in-plane/out-of-plane response of masonry structural panels », *Computers & Structures*, vol. 260, p. 106721, févr. 2022, doi: 10.1016/j.compstruc.2021.106721.
- [25] M. Sousamli, F. Messali, et J. G. Rots, « A total-strain based orthotropic continuum model for the cyclic nonlinear behavior of unreinforced brick masonry structures », *Numerical Meth Engineering*, vol. 123, n° 8, p. 1813-1840, avr. 2022, doi: 10.1002/nme.6917.
- [26] L. Pelà, M. Cervera, et P. Roca, « An orthotropic damage model for the analysis of masonry structures », *Construction and Building Materials*, vol. 41, p. 957-967, avr. 2013, doi: 10.1016/j.conbuildmat.2012.07.014.
- [27] P. B. Lourénço, R. De Borst, et J. G. Rots, « A plane stress softening plasticity model for orthotropic materials », *Int. J. Numer. Meth. Engng.*, vol. 40, n° 21, p. 4033-4057, nov. 1997, doi: 10.1002/(SICI)1097-0207(19971115)40:21<4033::AID-NME248>3.0.CO;2-0.
- [28] M. Ortiz et E. P. Popov, « Accuracy and stability of integration algorithms for elastoplastic constitutive relations », *International Journal for Numerical Methods in Engineering*, vol. 21, n° 9, p. 1561-1576, 1985, doi: 10.1002/nme.1620210902.

7 Appendix:

7.1 Appendix 1: Residual vector for each problem

- Tension behavior: $\{\psi\} = [\sigma_n^{n+1} \quad \dot{\lambda}_1]^T$
- $$\wp_1 \left\{ \begin{array}{l} R_{\sigma_n} = \sigma_n^{n+1} - \sigma_n^{trial} + E\dot{\lambda}_1 \\ R_{F_T} = \sigma_n^{n+1} - \bar{f}_t \end{array} \right.$$

$$[J]^T = \begin{bmatrix} \frac{\partial R_{\sigma_n}}{\partial \sigma_n^{n+1}} = 1 & \frac{\partial R_{\sigma_n}}{\partial \tau^{n+1}} = 0 & \frac{\partial R_{\sigma_n}}{\partial \dot{\lambda}_2} = E \tan \psi \\ \frac{\partial R_{\sigma_s}}{\partial \sigma_n^{n+1}} = 0 & \frac{\partial R_{\sigma_s}}{\partial \tau^{n+1}} = 1 & \frac{\partial R_{\sigma_s}}{\partial \dot{\lambda}_2} = G \text{ sign} \\ \frac{\partial R_{F_S}}{\partial \sigma_n^{n+1}} = \tan \phi & \frac{\partial R_{F_S}}{\partial \tau^{n+1}} = \text{sign} & \frac{\partial R_{F_S}}{\partial \dot{\lambda}_2} = \textcolor{blue}{B} \end{bmatrix}$$

- Coupling between tension and shear:

- Shear behavior: $\{\psi\} = [\sigma_n^{n+1} \quad \tau^{n+1} \quad \dot{\lambda}_2]^T$
- $$\wp_2 \left\{ \begin{array}{l} R_{\sigma_n} = \sigma_n^{n+1} - \sigma_n^{trial} + E\dot{\lambda}_2 \tan \psi = 0 \\ R_{\sigma_s} = \tau^{n+1} - \tau^{trial} + G\dot{\lambda}_2 \cdot \text{sign}(\tau) = 0 \\ R_{F_S} = |\tau| + \sigma_n \tan \phi - f_s = 0 \end{array} \right.$$
- Coupling between tension and shear: $\{\psi\} = [\sigma_n^{n+1} \quad \tau^{n+1} \quad \dot{\lambda}_1^{n+1} \quad \dot{\lambda}_2^{n+1}]^T$
- $$\wp_3 \left\{ \begin{array}{l} R_{\sigma_n} = \sigma_n^{n+1} - \sigma_n^{trial} + K_n^0 \dot{\lambda}_1 + K_n^0 \dot{\lambda}_2 \tan \psi = 0 \\ R_{\sigma_s} = \tau^{n+1} - \tau^{trial} + K_s^0 \dot{\lambda}_2 \text{ sign} = 0 \\ R_{F_T} = \sigma_n^{n+1} - \bar{f}_t \\ R_{F_S} = |\tau^{n+1}| + \sigma_n^{trial} \tan \phi - f_s = 0 \end{array} \right.$$
- Compression behavior:
- $$\{\psi\} = [\sigma_n^{n+1} \quad \tau^{n+1} \quad \dot{\lambda}_3]^T$$
- $$\wp_4 \left\{ \begin{array}{l} R_{\sigma_n} = \sigma_n^{n+1} - \sigma_n^{trial} + 2K_n^0 \dot{\lambda}_3 C_{nn} \sigma_n^{n+1} = 0 \\ R_{\sigma_s} = \tau^{n+1} - \tau^{trial} + 2K_s^0 \dot{\lambda}_3 C_{ss} \sigma_s^{n+1} = 0 \\ R_{F_c} = C_{nn} (\sigma_n^{n+1})^2 + C_{ss} (\tau^{n+1})^2 + (\bar{\sigma}(\kappa_3))^2 = 0 \end{array} \right.$$
- Coupling between shear and compression: $\{\psi\} = [\sigma_n^{n+1} \quad \tau^{n+1} \quad \dot{\lambda}_2^{n+1} \quad \dot{\lambda}_3^{n+1}]^T$
- $$\wp_5 \left\{ \begin{array}{l} R_{\sigma_n} = \sigma_n^{n+1} - \sigma_n^{trial} + E(2\dot{\lambda}_3 \sigma_n^{n+1} C_{nn} + \dot{\lambda}_2 \tan \psi) = 0 \\ R_{\tau} = \tau^{n+1} - \tau^{trial} + G(2\dot{\lambda}_3 \sigma_s^{n+1} C_{ss} + \dot{\lambda}_2 \text{ sign}) = 0 \\ R_{F_S} = |\tau^{n+1}| + \sigma_n^{n+1} \tan \phi - f_s = 0 \\ R_{F_c} = C_{nn} (\sigma_n^{n+1})^2 + C_{ss} (\tau^{n+1})^2 + (\bar{\sigma}(\kappa_3))^2 = 0 \end{array} \right.$$

7.2 Appendix 2: Jacobian matrix for each problem

- Tension behavior:

$$[J]^T = \begin{bmatrix} \frac{\partial R_{\sigma_n}}{\partial \sigma_n^{n+1}} = 1 & \frac{\partial R_{\sigma_n}}{\partial \dot{\lambda}_1} = k_n \\ \frac{\partial R_{F_T}}{\partial \sigma_n^{n+1}} = 1 & \frac{\partial R_{F_T}}{\partial \dot{\lambda}_2} = \textcolor{blue}{A} \end{bmatrix}$$

- Shear behavior:

- Shear behavior: $\{\psi\} = [\sigma_n^{n+1} \quad \tau^{n+1} \quad \dot{\lambda}_2]^T$
- $$\wp_2 \left\{ \begin{array}{l} R_{\sigma_n} = \sigma_n^{n+1} - \sigma_n^{trial} + E\dot{\lambda}_2 \tan \psi = 0 \\ R_{\sigma_s} = \tau^{n+1} - \tau^{trial} + G\dot{\lambda}_2 \cdot \text{sign}(\tau) = 0 \\ R_{F_S} = |\tau| + \sigma_n \tan \phi - f_s = 0 \end{array} \right.$$
- Coupling between tension and shear:

$$J = \begin{bmatrix} J_{11} = \frac{\partial R_{\sigma_n}}{\partial \sigma_n^{n+1}} = 1 & J_{12} = \frac{\partial R_{\sigma_n}}{\partial \tau^{n+1}} = 0 & J_{13} = \frac{\partial R_{\sigma_n}}{\partial \dot{\lambda}_1} = k_n & J_{14} = \frac{\partial R_{\sigma_n}}{\partial \dot{\lambda}_2} = k_n \tan \psi \\ J_{21} = \frac{\partial R_{\sigma_s}}{\partial \sigma_n^{n+1}} = 0 & J_{22} = \frac{\partial R_{\sigma_s}}{\partial \tau^{n+1}} = 1 & J_{23} = \frac{\partial R_{\sigma_s}}{\partial \dot{\lambda}_1} = 0 & J_{24} = \frac{\partial R_{\sigma_s}}{\partial \dot{\lambda}_2} = k_s \text{ sign} \\ J_{31} = \frac{\partial R_{F_T}}{\partial \sigma_n^{n+1}} = 1 & J_{32} = \frac{\partial R_{F_T}}{\partial \tau^{n+1}} = 0 & J_{33} = \frac{\partial R_{F_T}}{\partial \dot{\lambda}_1} = \mathbf{A}_1 & J_{34} = \frac{\partial R_{F_T}}{\partial \dot{\lambda}_2} = \mathbf{A}_2 \\ J_{41} = \frac{\partial R_{F_S}}{\partial \sigma_n^{n+1}} = \tan \phi & J_{42} = \frac{\partial R_{F_S}}{\partial \tau^{n+1}} = \text{sign} & J_{43} = \frac{\partial R_{F_S}}{\partial \dot{\lambda}_1} = \mathbf{A}_3 & J_{44} = \frac{\partial R_{F_S}}{\partial \dot{\lambda}_2} = \mathbf{A}_4 \end{bmatrix}$$

- Compression behavior:

$$[J] = \begin{bmatrix} J_{11} = \frac{\partial R_{\sigma_n}}{\partial \sigma_n^{n+1}} = 1 + 2E\dot{\lambda}_3 C_{nn} & J_{12} = \frac{\partial R_{\sigma_n}}{\partial \tau^{n+1}} = 0 & J_{13} = \frac{\partial R_{\sigma_n}}{\partial \dot{\lambda}_3} = 2EC_{nn}\sigma_n^{n+1} \\ J_{21} = \frac{\partial R_{\sigma_s}}{\partial \sigma_n^{n+1}} = 0 & J_{22} = \frac{\partial R_{\sigma_s}}{\partial \tau^{n+1}} = 1 + 2G\dot{\lambda}_3 C_{ss} & J_{23} = \frac{\partial R_{\sigma_s}}{\partial \dot{\lambda}_3} = 2GC_{ss}\sigma_s^{n+1} \\ J_{31} = \frac{\partial R_F}{\partial \sigma_n^{n+1}} = 2C_{nn}\sigma_n^{n+1} & J_{32} = \frac{\partial R_F}{\partial \tau^{n+1}} = 2C_{ss}\sigma_s^{n+1} & J_{33} = \frac{\partial R_F}{\partial \dot{\lambda}_3} = \mathbf{A} \end{bmatrix}$$

- Coupling between shear and compression:

$$J = \begin{bmatrix} \frac{\partial R_{\sigma_n}}{\partial \sigma_n^{n+1}} = 1 + 2E\dot{\lambda}_3 C_{nn} & \frac{\partial R_{\sigma_n}}{\partial \sigma_s^{n+1}} = 0 & \frac{\partial R_{\sigma_n}}{\partial \dot{\lambda}_2} = E \tan \psi & \frac{\partial R_{\sigma_n}}{\partial \dot{\lambda}_3} = 2E\sigma_n^{n+1}C_{nn} \\ \frac{\partial R_{\sigma_s}}{\partial \sigma_n^{n+1}} = 0 & \frac{\partial R_{\sigma_s}}{\partial \sigma_s^{n+1}} = 1 + 2G\dot{\lambda}_3 C_{ss} & \frac{\partial R_{\sigma_s}}{\partial \dot{\lambda}_2} = G \text{ sign} & \frac{\partial R_{\sigma_s}}{\partial \dot{\lambda}_3} = 2G\tau^{n+1}C_{ss} \\ \frac{\partial R_{F_S}}{\partial \sigma_n^{n+1}} = \tan \phi & \frac{\partial R_{F_S}}{\partial \sigma_s^{n+1}} = \text{sign} & \frac{\partial R_{F_S}}{\partial \dot{\lambda}_2} = \mathbf{B}_1 & \frac{\partial R_{F_S}}{\partial \dot{\lambda}_3} = \mathbf{B}_2 \\ \frac{\partial R_{F_C}}{\partial \sigma_n^{n+1}} = 2\sigma_n^{n+1}C_{nn} & \frac{\partial R_{F_C}}{\partial \sigma_s^{n+1}} = 2\tau^{n+1}C_{ss} & \frac{\partial R_{F_C}}{\partial \dot{\lambda}_2} = \mathbf{B}_3 & \frac{\partial R_{F_C}}{\partial \dot{\lambda}_3} = \mathbf{B}_4 \end{bmatrix}$$

7.3 Appendix 3: necessary derivatives:

$$A = \frac{\partial R_{F_T}}{\partial \dot{\lambda}_2} = \left(\frac{\partial F_T}{\partial \{\sigma\}} + \frac{\partial F_T}{\partial \kappa_1} \frac{\partial \kappa_1}{\partial \{\sigma\}} \right)^T \frac{\partial \{\sigma\}}{\partial \dot{\lambda}_1} - \frac{\partial F_T}{\partial \kappa_1} \frac{\partial \kappa_1}{\partial \dot{\lambda}_1}$$

$$\frac{\partial F_T}{\partial \{\sigma\}} = 1 \quad \frac{\partial \kappa_2}{\partial \{\sigma\}} = 0 \quad \frac{\partial \{\sigma\}}{\partial \dot{\lambda}_1} = -k_n \quad \frac{\partial \kappa_1}{\partial \dot{\lambda}_1} = 1$$

➤ **Tension case:**

$$\frac{\partial F_T}{\partial \kappa_1} = \frac{\partial f_t}{\partial \kappa_1} = -\frac{f_t^2}{G_f^I} \exp\left(-\frac{f_t}{G_f^I} \kappa_1\right) \Rightarrow A = -k_n + \frac{f_t^2}{G_f^I} \exp\left(-\frac{f_t}{G_f^I} \kappa_1\right)$$

➤ **Shear Case:**

$$B = -k_n \tan \psi \tan \phi - k_s - \frac{\partial F_S}{\partial \kappa_2}$$

$$\frac{\partial F_S}{\partial \kappa_2} = \sigma_n \frac{\partial(\tan \phi)}{\partial \kappa_2} + \frac{\partial f_S}{\partial \kappa_2} = \frac{\partial f_S}{\partial \kappa_2} \left(\sigma_n \frac{\partial(\tan \phi)}{\partial f_S} + 1 \right) = -\frac{c^2}{G_f^{II}} \exp\left(\frac{c}{G_f^{II}} \kappa_2\right) \left(\sigma_n \frac{\tan \phi_r - \tan \phi_0}{c} + 1 \right)$$

➤ **Coupling shear and tension:** To calculate the expressions A_1, A_2, A_3 , and A_4 will use the relation:

$$\frac{\partial R}{\partial \dot{\lambda}} = \left(\frac{\partial F}{\partial \{\sigma\}} + \frac{\partial F_C}{\partial \kappa_i} \frac{\partial \kappa_i}{\partial \{\sigma\}} \right)^T \frac{\partial \{\sigma\}}{\partial \dot{\lambda}} - \frac{\partial F}{\partial \kappa_i} \frac{\partial \kappa_i}{\partial \dot{\lambda}_i} \quad \frac{\partial \kappa_2}{\partial \dot{\lambda}_1} = \frac{G_f^{II^2} \text{ft}^2}{G_f^{I^2} c^2} \frac{\dot{\lambda}_1}{\dot{\kappa}_2} \quad \frac{\partial \kappa_2}{\partial \dot{\lambda}_2} = \frac{\dot{\lambda}_2}{\dot{\kappa}_2}$$

$$\frac{\partial \kappa_1}{\partial \dot{\lambda}_1} = \frac{\dot{\lambda}_1}{\dot{\kappa}_1} \quad \frac{\partial \kappa_1}{\partial \dot{\lambda}_2} = \frac{G_f^{I^2} c^2}{G_f^{II^2} \text{ft}^2} \frac{\dot{\lambda}_2}{\dot{\kappa}_1} \quad \frac{\partial \{\sigma\}}{\partial \dot{\lambda}_i} = -\begin{pmatrix} k_n & k_n \tan \psi \\ 0 & k_s \text{ sign}(\tau) \end{pmatrix}$$

$$A_1 = -k_n - \frac{\partial \bar{f}_t}{\partial \dot{\kappa}_1} \frac{\dot{\lambda}_1}{\dot{\kappa}_1}$$

$$A_2 = -k_n \tan \psi - \frac{\partial \bar{f}_t}{\partial \dot{\kappa}_1} \frac{G_f^{I^2} c^2}{G_f^{II^2} \text{ft}^2} \frac{\dot{\lambda}_2}{\dot{\kappa}_1}$$

We denote: $P = \frac{\tan \phi_r - \tan \phi_0}{c}$

$$A_3 = -k_n \tan \phi - (\sigma_n P + 1) \frac{\partial \bar{f}_s}{\partial \dot{\kappa}_2} \frac{G_f^{II^2} \text{ft}^2}{G_f^{I^2} c^2} \frac{\dot{\lambda}_1}{\dot{\kappa}_2}$$

$$A_4 = -k_n \tan \phi \tan \psi - k_s - (\sigma_n P + 1) \frac{\partial \bar{f}_s}{\partial \dot{\kappa}_2} \frac{\dot{\lambda}_2}{\dot{\kappa}_2}$$

➤ Compression behavior:

$$A = \frac{\partial R_F}{\partial \dot{\lambda}_3} = \left(\frac{\partial F_C}{\partial \{\sigma\}} + \frac{\partial F_C}{\partial \kappa_3} \frac{\partial \kappa_3}{\partial \{\sigma\}} \right)^T \frac{\partial \{\sigma\}}{\partial \dot{\lambda}_3} - \frac{\partial F_C}{\partial \kappa_3} \frac{\partial \kappa_3}{\partial \dot{\lambda}_3}$$

With: (We note for the sake of simplicity $BB = \sqrt{(\sigma_n)^2 + (C_{ss}\sigma_s)^2}$):

$$\frac{\partial F_C}{\partial \kappa_3} = \frac{\partial F_C}{\partial \bar{\sigma}} \frac{\partial \bar{\sigma}}{\partial \kappa_3} = -2\bar{\sigma} \frac{\partial \bar{\sigma}}{\partial \kappa_3} = -2\bar{\sigma} A_1$$

$$A_1 = \begin{cases} \frac{\partial \bar{\sigma}_a}{\partial \kappa_3} = 2(\bar{\sigma}_p - \bar{\sigma}_i)\beta \left(\frac{1}{\kappa_p} - \frac{\kappa_3}{\kappa_p^2} \right) \left[\frac{2\kappa_3}{\kappa_p} - \left(\frac{2\kappa_3}{\kappa_p} \right)^2 \right]^{\beta-1} \\ \frac{\partial \bar{\sigma}_b}{\partial \kappa_3} = \frac{(\bar{\sigma}_m - \bar{\sigma}_p)}{\kappa_m - \kappa_p} \alpha \left(\frac{\kappa_3 - \kappa_p}{\kappa_m - \kappa_p} \right)^{\alpha-1} \\ \frac{\partial \bar{\sigma}_b}{\partial \kappa_3} = m \exp \left(m \frac{\kappa_3 - \kappa_m}{\bar{\sigma}_m - \bar{\sigma}_r} \right) \end{cases}$$

$$\frac{\partial \kappa_3}{\partial \{\sigma\}} = \frac{\dot{\lambda}_3}{BB} \left(\frac{C_{nn}^2 \sigma_n}{C_{ss}^2 \sigma_s} \right)$$

$$\frac{\partial \{\sigma\}}{\partial \dot{\lambda}_3} = \begin{pmatrix} -2K_n^0 C_{nn} \sigma_n^{n+1} \\ -2K_s^0 C_{ss} \sigma_s^{n+1} \end{pmatrix} \quad \frac{\partial \kappa_3}{\partial \dot{\lambda}_3} = 2BB$$

$$A = 4 \left\{ \begin{pmatrix} \left(1 - \bar{\sigma} A_1 \frac{\dot{\lambda}_3}{BB} C_{nn} \right) \\ \left(1 - \bar{\sigma} A_1 \frac{\dot{\lambda}_3}{BB} C_{ss} \right) \end{pmatrix}^T \begin{pmatrix} -\frac{k_n (C_{nn} \sigma_n^{n+1})^2}{1 + 2K_n^0 \dot{\lambda}_3 C_{nn}} \\ -\frac{k_s (C_{ss} \sigma_s^{n+1})^2}{1 + 2K_s^0 \dot{\lambda}_3 C_{ss}} \end{pmatrix} + \bar{\sigma} A_1 BB \right\}$$

➤ Coupling shear and compression:

To calculate the expressions B_1 , B_2 , B_3 , and B_4 will use the relation:

$$\sigma_n^{n+1} (1 + 2K_n^0 \dot{\lambda}_3 C_{nn}) - (\sigma_n^{trial})^{n+1} + K_n^0 \dot{\lambda}_2 \tan \psi = 0 \Rightarrow$$

$$\sigma_n^{n+1} = \frac{(\sigma_n^{trial})^{n+1} - K_n^0 \dot{\lambda}_2 \tan \psi}{1 + 2K_n^0 \dot{\lambda}_3 C_{nn}}$$

$$\tau^{n+1} (1 + 2K_s^0 \dot{\lambda}_3 C_{ss}) - (\sigma_s^{trial})^{n+1} + K_s^0 \dot{\lambda}_2 sign = 0 \Rightarrow$$

$$\tau^{n+1} = \frac{(\sigma_s^{trial})^{n+1} - K_s^0 \dot{\lambda}_2 sign}{1 + 2K_s^0 \dot{\lambda}_3 C_{ss}}$$

To calculate the expressions B_1 , B_2 , B_3 , and B_4 will use

the relation: $\frac{\partial R}{\partial \dot{\lambda}} = \left(\frac{\partial F}{\partial \{\sigma\}} + \frac{\partial F}{\partial \kappa_i} \frac{\partial \kappa_i}{\partial \{\sigma\}} \right)^T \frac{\partial \{\sigma\}}{\partial \dot{\lambda}} - \frac{\partial F}{\partial \kappa_i} \frac{\partial \kappa_i}{\partial \dot{\lambda}}$

Notice: $\dot{\kappa}_3 = 2\dot{\lambda}_3 \sqrt{(\sigma_n)^2 + (C_{ss}\sigma_s)^2}$ and $\dot{\kappa}_2 = \dot{\lambda}_2$ (because there is no coupling)

The necessary derivatives are:

$$\begin{aligned} \frac{\partial \kappa_2}{\partial \dot{\lambda}_2} &= 1 & \frac{\partial \kappa_2}{\partial \dot{\lambda}_3} &= \frac{\partial \kappa_3}{\partial \dot{\lambda}_2} = 0 \\ \frac{\partial \kappa_3}{\partial \dot{\lambda}_3} &= 2\sqrt{(\sigma_n)^2 + (C_{ss}\sigma_s)^2} & \frac{\partial F_S}{\partial \kappa_2} &= \frac{\partial F_S}{\partial \bar{f}_S} \frac{\partial \bar{f}_S}{\partial \kappa_2} = -\frac{\partial \bar{f}_S}{\partial \kappa_2} \\ \frac{\partial F_C}{\partial \kappa_3} &= \frac{\partial F_C}{\partial f_c} \frac{\partial f_c}{\partial \kappa_3} = -2f_c \frac{\partial f_c}{\partial \kappa_3} & \frac{\partial \kappa_3}{\partial \{\sigma\}} &= \frac{\dot{\lambda}_3}{2BB} \left(\frac{C_{nn}^2 \sigma_n}{C_{ss}^2 \sigma_s} \right) \end{aligned}$$

with $BB = \sqrt{(\sigma_n)^2 + (C_{ss}\sigma_s)^2}$

$$\frac{\partial \{\sigma\}}{\partial \dot{\lambda}_i} = - \begin{pmatrix} \frac{k_n \tan \psi}{1 + 2K_n^0 \dot{\lambda}_3 C_{nn}} & \frac{2k_n C_{nn} \sigma_n^{n+1}}{1 + 2K_n^0 \dot{\lambda}_3 C_{nn}} \\ \frac{k_s sign}{1 + 2K_s^0 \dot{\lambda}_3 C_{ss}} & \frac{2k_s C_{ss} \sigma_s^{n+1}}{1 + 2K_s^0 \dot{\lambda}_3 C_{ss}} \end{pmatrix}$$

From these derivatives, we obtain the coefficients A , B , C et D by:

$$B_1 = -\frac{k_n \tan \psi \tan \phi}{1 + 2K_n^0 \dot{\lambda}_3 C_{nn}} - \frac{k_s}{1 + 2K_s^0 \dot{\lambda}_3 C_{ss}} + \frac{\partial \bar{f}_s}{\partial \kappa_2}$$

$$B_2 = -\tan \phi \frac{2k_n C_{nn} \sigma_n^{n+1}}{1 + 2K_n^0 \dot{\lambda}_3 C_{nn}} - sign \frac{2k_s C_{ss} \sigma_s^{n+1}}{1 + 2K_s^0 \dot{\lambda}_3 C_{ss}}$$

$$B_3 = -2C_{nn} \sigma_n^{n+1} \frac{k_n \tan \psi}{1 + 2K_n^0 \dot{\lambda}_3 C_{nn}} - 2C_{ss} \sigma_s^{n+1} \frac{k_s sign}{1 + 2K_s^0 \dot{\lambda}_3 C_{ss}}$$

$$B_4 = 4 \left\{ \begin{pmatrix} \left(1 - \bar{\sigma} A_1 \frac{\dot{\lambda}_3}{BB} C_{nn} \right) \\ \left(1 - \bar{\sigma} A_1 \frac{\dot{\lambda}_3}{BB} C_{ss} \right) \end{pmatrix}^T \begin{pmatrix} -\frac{k_n (C_{nn} \sigma_n^{n+1})^2}{1 + 2K_n^0 \dot{\lambda}_3 C_{nn}} \\ -\frac{k_s (C_{ss} \sigma_s^{n+1})^2}{1 + 2K_s^0 \dot{\lambda}_3 C_{ss}} \end{pmatrix} + \bar{\sigma} A_1 BB \right\}$$

7.4 Appendix 4: Material parameters of model

DIANA	Physics	Signification	Unit
<i>Material parameters</i>			
USRVAL (1)	C_{ss}	Shear Contribution Parameter	/
USRVAL (2)	G_{fs}	Shear Fracture Energy	N/mm
USRVAL (3)	G_{ft}	Tensile Breaking Energy	N/mm
USRVAL (4)	G_{fc}	Compressive Fracture Energy	N/mm
USRVAL (5)	$\tan \phi_f$	Tangent of the final internal friction angle	/

USRVAL (6)	$\tan \phi_i$	Tangent of the initial internal friction angle	/
USRVAL (7)	f_t	Tensile strength	MPa
USRVAL (8)	c	Cohesion	MPa
USRVAL (9)	f_c	Compressive strength	MPa
USRVAL (10)	$\tan \psi$	Tangent of the dilatancy angle	/
<i>Internal variables</i>			
URSTA (1)	w_c	Compression damage	/
URSTA (2)	w	Tensile and shear damage	/
URSTA (3)	k_1	Tensile equivalent plastic deformation	mm
URSTA (4)	k_2	Shear equivalent plastic deformation	mm
URSTA (5)	k_3	Compression equivalent plastic deformation	mm

URSTA (6)	d_{max}	Max displacement before tensile discharge	mm
URSTA (7)	$pente$	Rigidity during secant discharge	MPa
URSTA (8)	d_{cum}	Cumulative Displacement for Intersecting Discharge	mm
<i>Constitutive Law</i>			
SE (1,1) SE (2,2)	E G	Stiffness matrix	MPa
DU	$\{de, d_{g1}, d_{g2}\}$	Increment displacement vector	mm
TRA	$\{\sigma, \tau_s, \tau_t\}$	Tensile stress vector	MPa
STIFF _{2*2or3*3}	L_{tan}	Tangent Operator (Matrix)	MPa